Atmosphere–Ocean Coupled Energy Budgets of Tropical Convective Discharge–Recharge Cycles

BRANDON WOLDING,[a] ADAM RYDBECK,[b] JULIANA DIAS,[c] FIAZ AHMED,[d] MARIA GEHNE,[a] GEORGE KILADIS,[c] EMILY M. RILEY DELLARIPA,[e] XINGCHAO CHEN,[f] AND ISABEL L. MCCOY[a,g]

[a] *Cooperative Institute for Research in Environmental Sciences, University of Colorado Boulder, Boulder, Colorado*
[b] *U.S. Naval Research Laboratory, Stennis Space Center, Mississippi*
[c] *National Oceanic and Atmospheric Administration/Physical Sciences Laboratory, Boulder, Colorado*
[d] *Department of Atmospheric and Oceanic Sciences, University of California, Los Angeles, Los Angeles, California*
[e] *Department of Atmospheric Science, Colorado State University, Fort Collins, Colorado*
[f] *Department of Meteorology and Atmospheric Science, Center for Advanced Data Assimilation and Predictability Techniques, The Pennsylvania State University, University Park, Pennsylvania*
[g] *National Oceanic and Atmospheric Administration/Chemical Sciences Laboratory, Boulder, Colorado*

(Manuscript received 4 April 2023, in final form 19 October 2023, accepted 26 October 2023)

ABSTRACT: An energy budget combining atmospheric moist static energy (MSE) and upper ocean heat content (OHC) is used to examine the processes impacting day-to-day convective variability in the tropical Indian and western Pacific Oceans. Feedbacks arising from atmospheric and oceanic transport processes, surface fluxes, and radiation drive the cyclical amplification and decay of convection around suppressed and enhanced convective equilibrium states, referred to as shallow and deep convective discharge–recharge (D–R) cycles, respectively. The shallow convective D–R cycle is characterized by alternating enhancements of shallow cumulus and stratocumulus, often in the presence of extensive cirrus clouds. The deep convective D–R cycle is characterized by sequential increases in shallow cumulus, congestus, narrow deep precipitation, wide deep precipitation, a mix of detached anvil and altostratus and altocumulus, and once again shallow cumulus cloud types. Transitions from the shallow to deep D–R cycle are favored by a positive "column process" feedback, while discharge of convective instability and OHC by mesoscale convective systems (MCSs) contributes to transitions from the deep to shallow D–R cycle. Variability in the processes impacting MSE is comparable in magnitude to, but considerably more balanced than, variability in the processes impacting OHC. Variations in the quantity of atmosphere–ocean coupled static energy (MSE + OHC) result primarily from atmospheric and oceanic transport processes, but are mainly realized as changes in OHC. MCSs are unique in their ability to rapidly discharge both lower-tropospheric convective instability and OHC.

KEYWORDS: Convective clouds; Energy transport; Madden-Julian oscillation; Intraseasonal variability; Oceanic variability; Tropical variability

1. Introduction

Each day solar insolation warms the upper tropical oceans, from which heat and moisture are transferred to the lower atmosphere via turbulent fluxes, warming, moistening, and increasing the moist static energy (MSE) of planetary boundary layer air (Randall 2015). Convective updrafts carry high MSE boundary layer air into the free troposphere, condensing water vapor to form precipitation and clouds, which shade the ocean from solar insolation, and trap outgoing longwave radiation in the atmosphere. Latent heat released within convective updrafts helps drive the atmospheric circulation which, in turn, influences ocean currents and mixing. Atmospheric and oceanic motions spatially redistribute heat, moisture, and momentum over a wide range of scales.

When considered at sufficiently large spatial and temporal scales, these processes can be characterized by various forms of statistical quasi balance (Arakawa and Schubert 1974; Raymond 1997; Neelin et al. 2008; Jakob et al. 2019). In the tropics, convective activity is uniquely and intimately linked to atmospheric transports of MSE through weak temperature gradient (WTG) balance (Sobel and Bretherton 2000; Sobel et al. 2001; Raymond 2001). Raymond et al. (2009) suggested that if the efficiency of MSE export by atmospheric transport processes is an increasing function of convective activity, then the tropical atmosphere may behave like a bistable system, with a humid, enhanced convective equilibrium state separated from a dry, suppressed convective equilibrium state by an unstable equilibrium state (appendix A, Fig. A1). Multiple-equilibria studies applying the WTG approximation to both single-column atmospheric models with parameterized convection and cloud permitting models have documented initial condition dependence of convective evolution that is broadly consistent with a bistable system having two basins of attraction adjoined by an unstable equilibrium, akin to a skateboard park with two bowls separated by a narrow spine (Sobel et al. 2007; Sessions et al. 2010).

Denotes content that is immediately available upon publication as open access.

Corresponding author: Brandon Wolding, brandon.wolding@noaa.gov

DOI: 10.1175/JAS-D-23-0061.1

Previous studies examining day-to-day convective variability indicate that, instead of being maintained near these states of quasi equilibrium, coupled feedbacks between clouds and their surrounding environment give rise to the cyclical amplification and decay of convection, referred to as convective discharge–recharge (D–R) cycles (Bladé and Hartmann 1993; Yano and Plant 2012a; Hannah et al. 2016; Igel 2017; Inoue and Back 2017; Wolding et al. 2020a; Yano et al. 2020; Maithel and Back 2022). These studies suggest that D–R cycles are ubiquitous over tropical oceans, and occur on time scales of approximately 10–40 days (Inoue et al. 2021; Maithel and Back 2022). Observations indicate that the amplification of convection is characterized by a transition from predominantly shallow, to convective, to stratiform precipitation types, and increasing mesoscale convective system (MCS) activity (Hannah et al. 2016; Wolding et al. 2020a, 2022; Chen et al. 2022). During amplification, moistening begins in the boundary layer and moves progressively upward into the free troposphere, increasing column saturation fraction (CSF) and MSE, and is accompanied by a dipole of weak warming and cooling occurring above and below the freezing level, respectively (Igel 2017; Wolding et al. 2022).

The processes driving D–R cycles have been examined using field campaign data, various satellite products, and ERA-Interim (ERAi) (Masunaga and L'Ecuyer 2014; Hannah et al. 2016; Inoue and Back 2017; Inoue et al. 2021; Maithel and Back 2022). Using ERAi reanalysis, Inoue et al. (2021) found that the cyclical amplification and decay of convection was primarily explained by variability in horizontal moisture advection, in the absence of which convection self-amplified through a positive "column-process" feedback (i.e., net effect of vertical moisture advection, precipitation, and surface evaporation) (Chikira 2014). In contrast, using a mix of field campaign, satellite, and reanalysis data, Masunaga and L'Ecuyer (2014) and Maithel and Back (2022) found variability in vertical MSE advection to play a more equitable, or even dominant role, when compared to horizontal moisture advection. The individual roles of surface flux and radiative feedbacks were not clearly distinguished in these studies.

This study views D–R cycles as arising from two-way interactions between clouds and their surrounding environment. The dynamic and thermodynamic states of the atmosphere and upper ocean influence the amount, structure, and organization of clouds that are favored. Clouds, in turn, influence the dynamic and thermodynamic evolution of the atmosphere and upper ocean through their impacts on heat, moisture, and momentum transport, radiation, and surface fluxes. Here we focus on the thermodynamic aspects of D–R cycles, and aim to advance understanding in three key areas:

1) How the amount, structure, and organization of clouds evolve throughout D–R cycles
2) How the thermodynamic states of the atmosphere and upper ocean evolve throughout D–R cycles
3) Which processes drive the thermodynamic evolution of the atmosphere and upper ocean

Advancing understanding in these three areas is a requisite step to guiding coupled model development, improving weather prediction across a range of time scales, and informing future climate projections.

Section 2 describes data used in this study. In section 3, a plume model, which takes advantage of the full vertical structure of lower-tropospheric moisture and temperature variability, is used to identify D–R cycles. The goals of this study are then addressed sequentially in sections 4–6. In section 4, satellite-derived precipitation and cloud type datasets are used to characterize changes in the amount, structure, and organization of clouds throughout D–R cycles. The thermodynamic evolution of the atmosphere and upper ocean are examined in section 5, and the processes driving this evolution are examined using an atmosphere–ocean coupled energy budget in section 6. In section 7, a preliminary examination of the Dynamics of the Madden–Julian Oscillation (DYNAMO) field campaign is used to illustrate and integrate concepts discussed in previous sections (Yoneyama et al. 2013; Zhang 2013). Discussion is provided in section 8, and summary and conclusions are provided in section 9. By using an incrementally more sophisticated measure of convective instability to identify D–R cycles, and by using an atmosphere–ocean coupled energy budget to examine the processes driving D–R cycles, this study serves as a natural extension of prior D–R cycle research.

2. Data

Unless otherwise noted, data are regridded from their native resolution to a common 2.5° × 2.5° horizontal grid, averaged to daily temporal resolution, and limited to the tropical Indian and west Pacific Oceans (10°N–10°S, 60°–170°E) for the time period 2001–15. Previous studies have shown that while D–R cycles are ubiquitous across the tropics, the processes driving these cycles vary geographically (Inoue and Back 2017; Inoue et al. 2021). The Indian and west Pacific Oceans are characterized by similar D–R processes and, importantly, offer more extensive in situ observations representative of oceanic conditions (e.g., field campaign data, small island sounding records) than other regions of the tropics. As many of the datasets described below have been documented extensively elsewhere, here descriptions will be limited to highlight aspects of the data most relevant to this study, with pertinent citations provided for the interested reader.

a. ERA5 atmosphere and HYCOM ocean reanalyses

European Centre for Medium-Range Weather Forecasts version 5 reanalysis (ERA5) data including specific humidity, temperature, geopotential height, zonal winds, shortwave radiative heating, longwave radiative heating, surface sensible heat flux, and surface latent heat flux are used for the calculation of the MSE budget and as input to the numerical plume model (Hersbach et al. 2020). Hybrid Coordinate Ocean Model (HYCOM) data including ocean temperature and horizontal ocean current are used for the calculation of the ocean heat content (OHC) budget. While HYCOM reanalysis uses surface forcing fields from the National Centers for Environmental

Prediction Climate Forecast System Reanalysis, ERA5 surface forcing fluxes are used in both the MSE and OHC budgets for consistency in the atmosphere–ocean coupled budget. Comparisons of HYCOM and ERA5 surface forcings indicate that the primary conclusions of this study are not qualitatively impacted by differences between these products. MSE and OHC budget terms are calculated using the regridded, daily average data. MSE vertical advection is calculated as the MSE budget residual, and the sum of OHC vertical advection, OHC horizontal diffusion, and OHC vertical diffusion are calculated as the residual of the OHC budget. Section 3 of Wolding and Maloney (2015) discusses motivations for calculating MSE vertical advection as the MSE budget residual, and explicit calculation of MSE vertical advection does not qualitatively impact the primary conclusions of this study.

b. *IMERG precipitation and mesoscale convective system classification*

Integrated Multi-satellitE Retrievals for GPM (IMERG) precipitation V06 (Huffman et al. 2015; Tan et al. 2019), which spans the entire analysis period, is the primary precipitation dataset used in this study. Additionally, an MCS tracking precipitation dataset developed by Feng et al. (2021), which decomposes IMERG precipitation into contributions from MCS, non-MCS deep, and nondeep precipitation types (described below), is used in section 4b. MCS tracking data are restricted to the time period of 2001–14, excluding years 2003–05, because frequently missing infrared (IR) brightness temperature (Tb) data during the excluded time period made MCS tracking in the western Pacific unreliable (Feng et al. 2021).

MCS classification begins by identifying cold cloud systems (CCSs) using NASA global merged IR V1 Tb data (Janowiak et al. 2017), whereby cold cloud cores (Tb $<$ 225 K) are iteratively grown outwards to reach 241 K, and tracked if the overlapping area between two successive hourly Tb observations exceeds 50%. IMERG precipitation features (PFs) are then matched to CCSs, and classified as MCS precipitation if the CCS is sufficiently large (>40 000 km^2) and long lived (>4 h), and PF characteristics (e.g., rain rate, rain area, major axis length) exceed thresholds defined in Feng et al. (2021). Precipitating CCSs that do not meet the MCS criteria are classified as non-MCS deep precipitation, and precipitating cloud systems that do not meet CCS criteria are defined as nondeep precipitation.

c. CloudSat *cloud type data*

The *CloudSat* cloud type database developed by Riley and Mapes (2009) and Riley et al. (2011) is limited to the years 2006–10, as a 2011 battery failure limited subsequent operation to daytime overpasses. Echo objects (EOs) are identified as contiguous regions (>3 pixels) of cloudiness (cloud mask $>$ 20), and then assigned a cloud type, which is determined by the EO base altitude, the EO top altitude, as well as the EO width. Cloud types are delineated using 4.5 and 10 km EO top thresholds, which separate warm, potentially mixed-phase, and fully glaciated EO tops (Riley and Mapes 2009). Additional EO bottom thresholds of 3 and 7 km are used to delineate geometrically thicker and thinner clouds. Cloud types are cumulus (CU; top $\leq$ 4.5 km, width $\leq$ ~10 km), stratocumulus (SCU; top $\leq$ 4.5 km, width $>$ ~10 km), cumulus congestus (CG; base $<$ 3 km, 4.5 $<$ top $\leq$ 10 km), altostratus and altocumulus (ASAC; base $\geq$ 3 km, 4.5 $<$ top $\leq$ 10 km), narrow deep precipitation (NDP; base $<$ 3 km, top $>$ 10 km, width $\leq$ ~20 km), wide deep precipitation (WDP; base $<$ 3 km, top $>$ 10 km, width $>$ ~200 km), detached anvil (DAN; 3 km $\geq$ base $<$ 7 km, top $>$ 10 km) and cirrus (CI; base $\geq$ 7 km, top $>$ 10 km). Mean EO latitude and longitude are then used to associate each EO with corresponding ERA5 and IMERG data on the common 2.5° × 2.5° horizontal grid.

d. *DYNAMO northern sounding array averaged data*

Northern sounding array (NSA) averaged estimates of specific humidity, temperature, and precipitation from the DYNAMO field campaign are obtained from the Colorado State University (CSU) quality-controlled version 3b DYNAMO dataset, available from 1 October to 31 December 2011 (Johnson and Ciesielski 2013; Ciesielski et al. 2014a,b; Johnson et al. 2015). In version 3b, observations are supplemented with ECMWF operational analysis in data-sparse regions and/or time periods. As discussed in section 7, the time period following the end of the CSU V3 DYNAMO dataset is also of interest. To extend the DYNAMO analysis for the month of January 2012, ERA5, HYCOM, and IMERG precipitation data, described in sections 2a and 2b, respectively, are averaged over the NSA. Comparisons of precipitation rate and $\langle B \rangle_{\mathrm{DIB}}$ (described in section 3) calculated from these data and CSU V3b data result in Pearson's correlation coefficients of 0.98 and 0.95, respectively, for the time period of 1 October–31 December 2011. While not examined in this study, we emphasize that legacy DYNAMO datasets offer observationally constrained estimates of atmosphere and ocean energy budget terms that could support future process-level studies (Johnson and Ciesielski 2013; Sobel et al. 2014; de Szoeke et al. 2015; Chen et al. 2016; Johnson and Ciesielski 2017).

3. Using lower-tropospheric vertically integrated buoyancy to identify convective discharge–recharge cycles

a. *Calculation of lower-tropospheric vertically integrated buoyancy*

Observational and modeling studies have shown convective onset and variability to be closely linked to various measures of lower-tropospheric convective instability, suggesting that such measures may prove useful for investigations of D–R cycles (Kuang 2008; Raymond et al. 2011; Ahmed and Neelin 2018; Adames et al. 2021). In this study, a plume model, which has been extensively utilized in studies of tropical convection, is used to calculate lower-tropospheric (1000–600 hPa) vertically integrate buoyancy ($\langle B \rangle$) (Holloway and Neelin 2009; Schiro et al. 2018, 2020; Ahmed and Neelin 2021). One benefit of limiting $\langle B \rangle$ computations to below the climatological freezing level (~575 hPa) is that it circumvents poorly

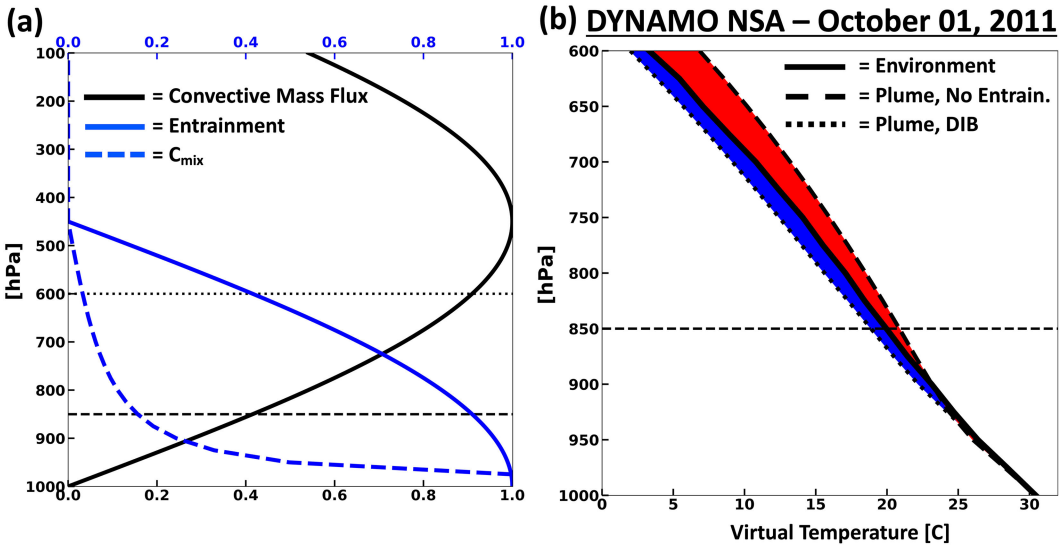

FIG. 1. (a) Deep-inflow B (DIB) convective mass flux (m; black line) and entrainment profiles (dm/dz; blue solid line), normalized by their maximum respective values. Mixing coefficient (C_{mix}; blue dashed line) for 25 hPa vertical resolution. (b) DYNAMO V3b NSA average virtual temperature profile from 1 Oct 2011 (solid line) and virtual temperature estimates for nonentraining (dashed line) and DIB entraining (dotted line) plumes. $\langle B\rangle_{\text{NOMIX}}$ (red shading) and $\langle B\rangle_{\text{DIB}}$ (blue shading) are shown as the vertically integrated difference between their respective plume profiles and the NSA average environment profile.

constrained assumptions relating to frozen precipitation processes (Johnson et al. 1999).

Vertical profiles of large-scale average (2.5° × 2.5°), daily average ERA5 specific humidity and temperature are input into the plume model, and used as both the initial properties of the "plume" (i.e., parcel), as well as the "environment" with which it mixes. Each plume is initiated at 1000 hPa, a level that broadly corresponds to the subcloud mixed layer, which observations estimate to be present ~70% of the time in the tropical Indian and west Pacific Oceans (Johnson et al. 2001; Johnson and Ciesielski 2017). As the plume "rises" (i.e., is lifted) above 1000 hPa, it mixes with environmental air according to the user prescribed entrainment profiles. Two different entrainment profiles are prescribed to the plume model: a "deep-inflow B" profile (DIB) where entrainment occurs over the entire depth of the lower troposphere, and a profile where no entrainment occurs (NOMIX). Considerable observational and modeling evidence indicates that lateral inflow of environmental air into both isolated and mesoscale organized convective plumes occurs over a deep layer of the lower troposphere (i.e., "deep inflow"), though specifics relating to the vertical structure of inflow rates, and the dependence of inflow rates on the dynamic and thermodynamic environment (e.g., wind shear, saturation deficit) are not well constrained (Kingsmill and Houze 1999; Mechem et al. 2002; McGee and Van den Heever 2014; Schiro et al. 2018; Peters et al. 2020, 2021; Kuo and Neelin 2022).

DIB entrainment corresponds to a sinusoidal convective mass flux profile having a peak at 450 hPa (Fig. 1a, black line), below which zero detrainment is assumed. Entrainment is therefore proportional to the rate of increase of convective mass flux with height, such that the mass contribution of environmental air entrained into the plume decreases with height (Fig. 1a, blue solid line), with detrainment occurring above 450 hPa as convective mass flux decreases with height. Computationally, a mixing coefficient C_{mix} (Fig. 1a, blue dashed line) is calculated at each vertical level k above the launch level following

$$C_{\text{mix}}(k) = \frac{m(k+1) - m(k-1)}{m(k+1) + m(k-1)}, \tag{1}$$

where m is convective mass flux. The coefficient C_{mix}, a discretized version of entrainment whose values are resolution dependent, is set to zero above the level of peak convective mass flux (450 hPa). Plume values of a conserved variable r are then calculated following

$$r_{\text{plume}}(k) = r_{\text{plume}}(k-1) \times [1 - C_{\text{mix}}(k)] + r_{\text{environment}}(k) \times C_{\text{mix}}(k), \tag{2}$$

where $r_{\text{plume}}(1000\text{ hPa}) = r_{\text{environment}}(1000\text{ hPa})$. Mixing is local, complete, and instantaneous. Ice–liquid water potential temperature is conserved during phase change (Bryan and Fritsch 2004), and liquid water exceeding 1 g kg^{-1} is rained out.

The plume computation yields a vertical profile of plume virtual temperature, which can then be used to estimate $\langle B\rangle$ following

$$\langle B\rangle = \int_{1000\text{hPa}}^{600\text{hPa}} R_d(T_{v,p} - T_{v,e})d\ln p, \tag{3}$$

where $T_{v,p}$ and $T_{v,e}$ are the virtual temperature of the plume and environment, respectively, and R_d is the gas constant for air, as in measures of convective available potential energy (CAPE) or convective inhibition (CIN) (Zhang 2009). The impacts of entrainment on $\langle B \rangle$ can then be estimated following

$$\langle B \rangle_{\text{MODENTRAIN}} = \langle B \rangle_{\text{DIB}} - \langle B \rangle_{\text{NOMIX}}, \tag{4}$$

where subscripts DIB and NOMIX indicate computations of $\langle B \rangle$ using DIB and NOMIX entrainment profiles, respectively.

An example of the plume model for the DYNAMO NSA on 1 October 2011 is provided in Fig. 1b. Virtual temperature profiles averaged over the DYNAMO NSA (solid line), for the NOMIX plume (dashed line), and for the DIB plume (dotted line) are shown in black lines. $\langle B \rangle_{\text{NOMIX}}$ (red shading) and $\langle B \rangle_{\text{DIB}}$ (blue shading) are shown as the integrated difference between their respective profiles and the DYNAMO NSA "environment" profile, and $\langle B \rangle_{\text{MODENTRAIN}}$ is the integrated difference between the DIB (dotted line) and NOMIX (dashed line) plume virtual temperature profiles.

Characteristic profiles of convective mass flux and associated entrainment are known to vary geographically and throughout D–R cycles (Schumacher et al. 2004; Back and Bretherton 2006; Kumar et al. 2015; Raymond and Fuchs-Stone 2021; Inoue et al. 2021). As $\langle B \rangle_{\text{DIB}}$ implements a fixed entrainment profile that is characteristic of deep convection, it should be viewed as a coarse estimate of the ability of the large-scale thermodynamic environment to support deep convection. We emphasize that large-scale average, daily average fields are used to determine both the initial properties of the plume, as well as the environment with which it mixes, *thereby neglecting variability on smaller spatiotemporal scales*. In reality, the existence of smaller-scale thermodynamic variability results in convective-scale $\langle B \rangle_{\text{DIB}}$ being distributed about the large-scale daily average estimate of $\langle B \rangle_{\text{DIB}}$, with few deep convective elements being supported at very negative values of large-scale $\langle B \rangle_{\text{DIB}}$, and deep convection becoming more widespread as large-scale $\langle B \rangle_{\text{DIB}}$ approaches positive values. Additional discussion of smaller-scale variability is provided in section 8.

b. Identification of convective discharge–recharge cycles

Convective D–R cycles can be broadly defined as the cyclical amplification and decay of convection coupled to cyclical increases and decreases in some relevant measure of convective instability, which is chosen to be $\langle B \rangle_{\text{DIB}}$ in this study. Several approaches have been used to identify and examine D–R cycles, each having respective strengths and weaknesses, and providing different perspectives of D–R cycles (see section 8 for further discussion). In this study, D–R cycles are initially identified by examining the temporal coevolution of precipitation rate and $\langle B \rangle_{\text{DIB}}$, and then further distinguished through analysis of thermodynamic tendencies and energy budgets. This approach is chosen because, among other reasons, it provides a relatively clear separation between shallow and deep convective D–R cycles, their respective cloud populations, and associated processes.

When considered over the Indian and west Pacific Oceans, the pdf of $\langle B \rangle_{\text{DIB}}$ (Fig. 2a, dashed line) has a single mode near ~ -100 J kg^{-1}, with a relatively long left tail, and a relatively short right tail. Viewed from a convective quasi-equilibrium (QE) perspective, the relatively long left tail could be considered the result of large-scale "forcings" (e.g., surface fluxes, radiative cooling) slowly driving the atmosphere toward a "critical point" of convective instability, beyond which increasingly widespread convection rapidly removes convective instability, resulting in the relatively short right tail (Peters and Neelin 2006). The joint distribution of precipitation and $\langle B \rangle_{\text{DIB}}$ is similarly characterized by a single mode (Fig. 2b, color shading), which occurs near ~ -100 J kg^{-1} and ~ 10 mm day^{-1}. The mode (i.e., most common state of the system) of various measures of convective instability has been shown to occur near the critical point, and could be viewed as arising from a quasi or statistical balance between the processes impacting convective instability and convection (Neelin et al. 2008). While bin-mean IMERG precipitation rate (Fig. 2a, solid line) increases with increasing $\langle B \rangle_{\text{DIB}}$, the joint distribution (Fig. 2b, color shading) indicates considerable spread around this bin-mean relationship, with precipitation rates varying two to three orders of magnitude for most $\langle B \rangle_{\text{DIB}}$ values.

To consider the day-to-day coupled evolution of precipitation rate and $\langle B \rangle_{\text{DIB}}$, data in Fig. 2b are binned along both axes, and the bin-mean temporal center differences of both precipitation rate and $\langle B \rangle_{\text{DIB}}$ are plotted as vectors, with vector tails at corresponding bin centers (Inoue and Back 2017; Wolding et al. 2020a). Note that the log precipitation scale results in the Y component of vectors becoming emphasized at low precipitation rates, and deemphasized at higher precipitation rates. Vectors, which represent the mean temporal coevolution of precipitation and $\langle B \rangle_{\text{DIB}}$ over a 2 day period, indicate two regions of cyclical behavior, which appear to overlap near ~ -200 J kg^{-1}. As the region of clockwise cyclical behavior is characterized by much lower precipitation rates than the region of counterclockwise cyclical behavior, these regions will hereafter be referred to as the shallow convective and deep convective D–R cycles, respectively. Further motivation for this interpretation is provided in section 4.

The two D–R cycles become more evident when the probabilities of increasing (warm colors) or decreasing (cool colors) precipitation rate (Fig. 3a), $\langle B \rangle_{\text{DIB}}$ (Fig. 3b), and CSF (Fig. 3c) are considered. Bin-mean tendencies (vectors) and probabilities (color shading) are in general agreement, showing two distinct regions of increasing precipitation rate and increasing $\langle B \rangle_{\text{DIB}}$ below and above ~ -250 and ~ -150 J kg^{-1}, respectively, separated by a region of decreasing precipitation rates for $\langle B \rangle_{\text{DIB}}$ values between -250 and -150 J kg^{-1}. Bin-mean probabilities (Fig. 3, color shading) are typically between 40% and 60%, indicating that variations in $\langle B \rangle_{\text{DIB}}$ and precipitation rate are not highly deterministic, and frequently depart from the cyclical trajectories of the bin-mean tendencies (vectors) (Yano et al. 2020). Residence times within one D–R cycle, before transitioning between cycles, average 5–30 days (appendix B). Transitions between D–R cycles are discussed in subsequent sections.

To facilitate subsequent discussion, Fig. 4 illustrates regions associated with the shallow convective D–R cycle (S1, S2), the deep convective D–R cycle (D1, D2, D3), and transitional

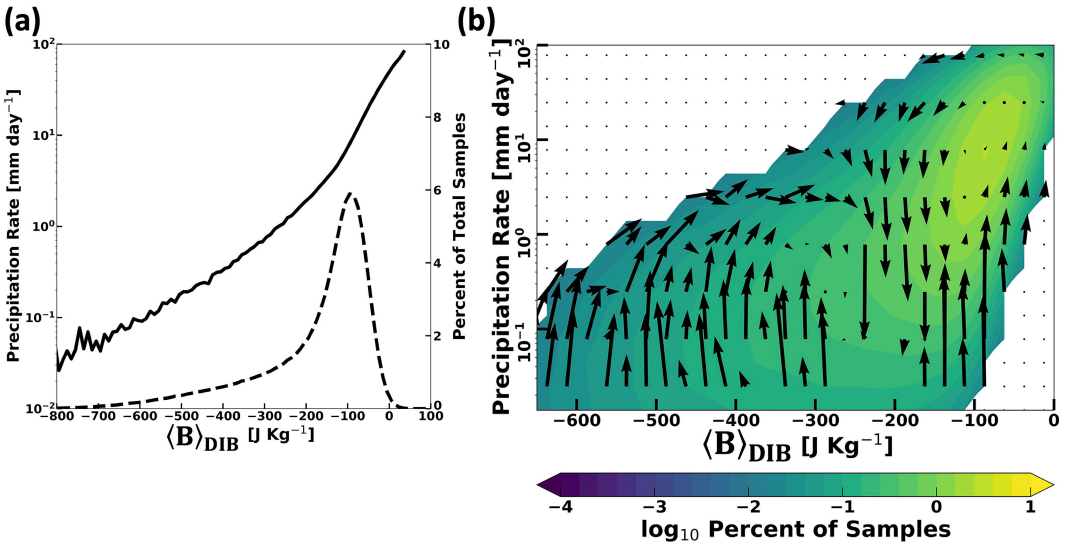

FIG. 2. (a) Bin-mean IMERG precipitation rate (solid black line; left Y axis; log scale) as a function of ERA5 $\langle B \rangle_{\mathrm{DIB}}$, and the PDF of $\langle B \rangle_{\mathrm{DIB}}$ (dashed black line; right Y axis). $\langle B \rangle_{\mathrm{DIB}}$ bin width is 10 J kg^{-1}. (b) Joint distribution (color shading; log scale) of IMERG precipitation (Y axis; log scale) and ERA5 $\langle B \rangle_{\mathrm{DIB}}$ (X axis). Vectors indicate the temporal coevolution of precipitation and $\langle B \rangle_{\mathrm{DIB}}$, calculated as their respective bin-mean temporal centered differences. Vector tails are plotted at bin centers. Note the log precipitation scale results in the Y component of vectors becoming emphasized at low precipitation rates, and deemphasized at high precipitation rates. Vectors extending to precipitation rates $< 10^{-2}$ mm day^{-1} are not plotted for clarity. Stippling denotes bins containing less than 200 samples, which are not plotted. $\langle B \rangle_{\mathrm{DIB}}$ bins are of width 25 J kg^{-1}, and 28 equally spaced log-precipitation rate bins spanning 10^{-4}–10^{3} mm day^{-1} are used.

regimes (T1, T2), which are distinguished from each other by their cloud population, thermodynamic tendencies, and/or atmosphere–ocean coupled energy budgets. Subsequent sections will show that transitional regimes (T1, T2) may be preceded by either shallow (S2) or deep convective conditions (D3); therefore, analyses of these transitional regimes must be interpreted with caution, as the cloud populations and associated processes are likely to depend on antecedent conditions (i.e., having transitioned from S2 or D3).

4. Characterizing the cloud population of convective discharge–recharge cycles

In this section, satellite-derived cloud type and precipitation type datasets are used to characterize how the amount, structure, and mesoscale organization of clouds evolve throughout D–R cycles. These characteristics are of particular interest because of their documented impacts on atmospheric transports of MSE, radiative heating, and surface fluxes, which are discussed below and examined in section 6.

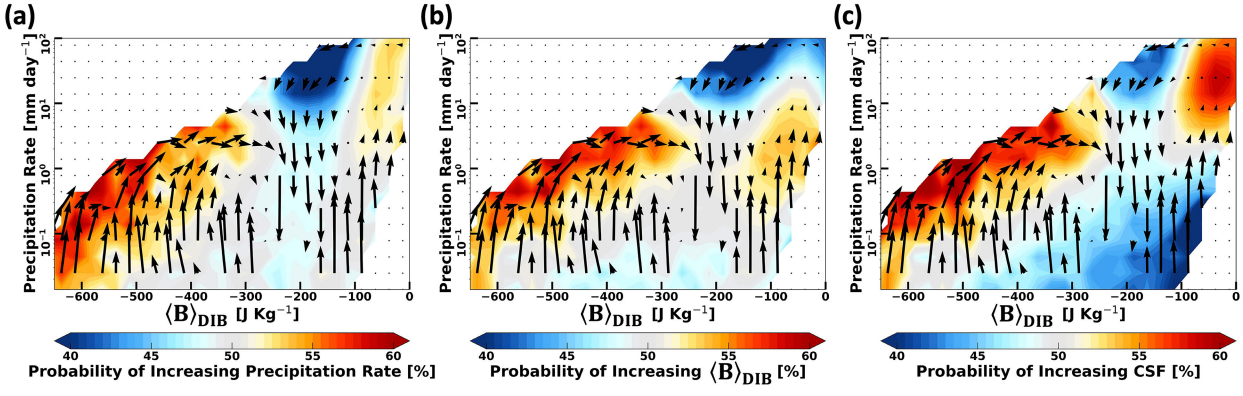

FIG. 3. As in Fig. 2b, except color shading shows the probability of increasing (a) precipitation rate, (b) $\langle B \rangle_{\mathrm{DIB}}$, and (c) column saturation fraction (CSF). The probability of increasing is calculated as the fraction of samples within each bin having a positive temporal centered difference.

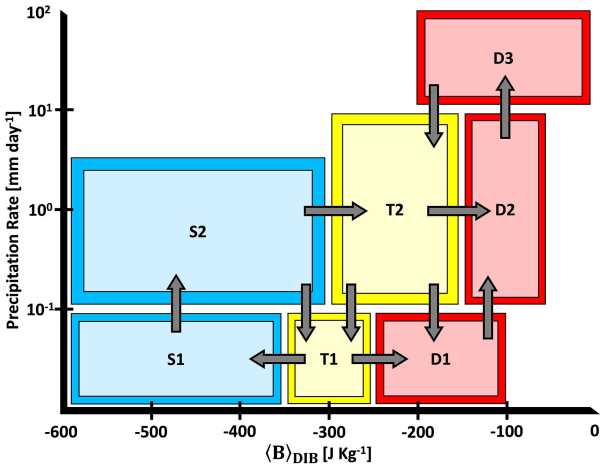

FIG. 4. Illustration of regions associated with the shallow convective D–R cycle (S1, S2), the deep convective D–R cycle (D1, D2, D3), and transitional regimes (T1, T2). Boundaries between regions are approximate.

a. CloudSat *cloud types*

CloudSat's cloud profiling radar, which is capable of detecting smaller cloud liquid and ice particles than the aforementioned precipitation radar products, provides a unique and relatively nuanced assessment of how cloud type and horizontal cloud coverage evolve throughout convective D–R cycles. In Fig. 5, EOs (see section 2) are conditionally binned using the "nearest" (in space and time) 2.5° × 2.5° daily average ERA5 $\langle B\rangle_{\mathrm{DIB}}$ and IMERG precipitation rate values (X and Y axes of subplots, respectively), and the composition of EO cloud types within each bin is shown in color shading.

The deep convective D–R cycle is characterized by the following sequence of changes. Increasing precipitation rates (Fig. 3a, upward vectors and warm colors) are accompanied by sequential increases in shallow cumulus, congestus, narrow deep precipitation, and wide deep precipitation cloud types (Fig. 5, D1–D3). Increasing $\langle B\rangle_{\mathrm{DIB}}$ (Fig. 3b, rightward vectors and warm colors) is associated with enhanced congestus (Fig. 5, D2), and increasing CSF (Fig. 3c, warm colors) is associated with the transition from congestus to narrow deep precipitation to wide deep precipitation (Fig. 5, D2, D3), which corresponds to the developing and mature phases of the MCS life cycle (Houze 2018, Figs. 17–22a,b). Enhanced wide deep precipitation is uniformly accompanied by decreasing $\langle B\rangle_{\mathrm{DIB}}$ (Fig. 3b, leftward vectors and cool colors, D3) and, as the proportion of narrow deep precipitation to wide deep precipitation decreases, precipitation rate and CSF begin decreasing (Figs. 3a,c, cool colors), corresponding to the decaying phase of the MCS life cycle (Houze 2018, Figs. 17–22c). Further decreases in precipitation rate and CSF are then accompanied by a mixture of altostratus/altocumulus and detached anvil, and a return to cumulus (Fig. 5, T2, T1, D1). A similar sequential progression is observed when considering the horizontal extent of EO cloudiness (appendix C, Fig. C1), though the relative contributions of wider cloud types (e.g., WDP) are enhanced when compared to EO composition (Fig. 5). This progression of cloud types characterizes a broad range of tropical convective variability, including the diurnal cycle, convectively coupled equatorial waves (CCEWS), and the Madden–Julian oscillation (e.g., Mapes et al. 2006, Fig. 11; Benedict and Randall 2007, Fig. 13; Kiladis et al. 2009, Fig. 19).

The shallow convective D–R cycle is characterized by the following sequence of changes. At precipitation rates $< \sim 0.1$ mm day^{-1}, cumulus make up ~45% of EOs (Fig. 5, S1). As precipitation rate, $\langle B\rangle_{\mathrm{DIB}}$, and CSF increase (Fig. 3, upward and rightward vectors, warm colors), cumulus decrease and more horizontally expansive stratocumulus increase (Fig. 5, S2). IMERG precipitation, examined in the next subsection, shows a deepening of convection during this cumulus to stratocumulus transition (Fig. 6), indicating the *CloudSat* stratocumulus clouds identified in this region more likely correspond to convective elements detraining between the trade inversion and the freezing level [e.g., cumulus rising into stratocumulus in decoupled boundary layers (Bretherton and Wyant 1997; Wood 2012), "gravel" or "flowers" in the trade winds (Bony et al. 2020a; Schulz et al. 2021)] than to stratocumulus topped boundary layers that are commonly observed near coasts in the subtropics but rarely seen in the study area (Wood 2012; McCoy et al. 2023). Congestus and altostratus/altocumulus increase as $\langle B\rangle_{\mathrm{DIB}}$ approaches -200 J kg^{-1} (Fig. 5, T2) and, as precipitation rates begin to decrease, stratocumulus decrease as cumulus once again increase (T1, S1). Interestingly, while the majority of EOs have tops that do not exceed 4.5 km, and therefore cannot detrain cloud water at upper levels, extensive amounts of cirrus with EO tops exceeding 10 km are present throughout the shallow convective D–R cycle (Figs. 5 and C1).

b. Mesoscale organization of deep convection

Deep convective clouds in close proximity can aggregate into MCSs, which induce circulations on scales larger than, and persist longer than, the individual updrafts and downdrafts from which they are composed (Moncrieff 2004; Houze 2018). MCSs are of particular interest because of their extensive impacts on MSE transports, radiation, and surface fluxes, as well as their limited representation in current weather and climate models. In MCSs, both convective-scale and mesoscale downdrafts transport low MSE downward from the midtroposphere, driving a net export of MSE from the column, while simultaneously drawing energy from the upper ocean in the form of enhanced surface fluxes (Zipser 1977; Esbensen and McPhaden 1996; Tobin et al. 2012). Additionally, the extensive stratiform anvils (>40 000 km^2) of MCSs greatly impact both LW and SW radiative heating (Houze 2018).

Figure 6 shows the fractional contributions (color shading) of nondeep, non-MCS deep, and MCS precipitation types to the total precipitation rate (Y axis). Nondeep precipitation is the dominant precipitation type at all precipitation rates $< \sim 10$ mm day^{-1}, irrespective of $\langle B\rangle_{\mathrm{DIB}}$ values. Non-MCS deep precipitation, which is often not sufficiently large and/or long lived enough to be classified as MCS precipitation,

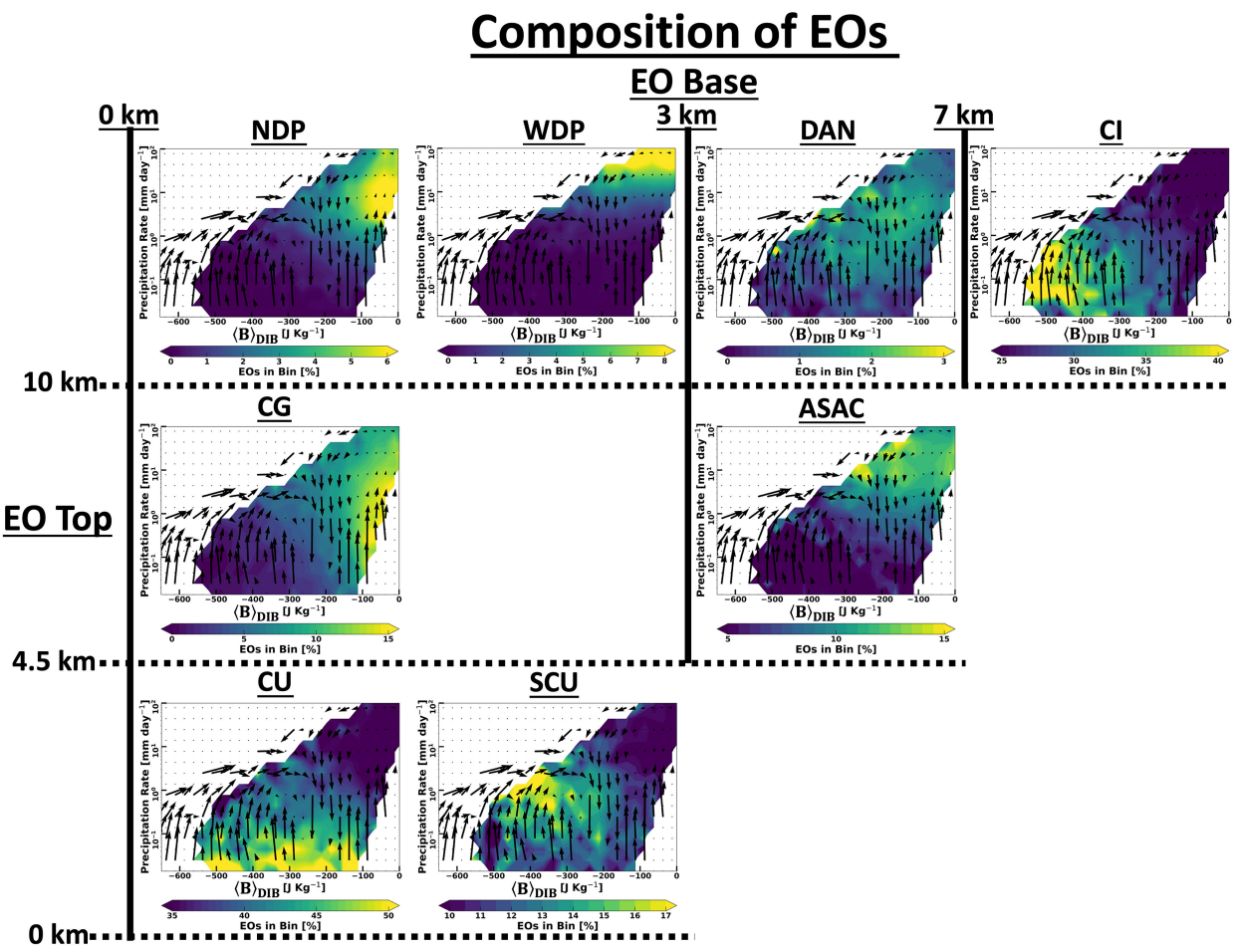

FIG. 5. As in Fig. 2b, except color shading shows the fraction of total EO in each bin identified as shallow cumulus (CU), stratocumulus (SCU), cumulus congestus (CG), altostratus and altocumulus (ASAC), narrow deep precipitation (NDP), wide deep precipitation (WDP), detached anvil (DAN), and cirrus (CI) cloud types. *CloudSat* EOs spans 2006–10, while vectors are calculated using IMERG precipitation and ERA5 thermodynamic fields from 2001 to 2015, as in Fig. 2b. Stippling denotes bins containing less than 100 samples, which are not plotted. Color scales do not have equal dynamic ranges.

accounts for approximately one-third of precipitation at rates between 1 and 10 mm day^{-1}. MCSs contribute the majority of precipitation at rates $> \sim$10 mm day^{-1} (D3); thus, large energetic changes are expected under these conditions (Chen et al. 2022). While MCSs appear to play little role in the shallow convective D–R cycle, changes in the mesoscale organization of deep convection are a fundamental feature of the deep convective D–R cycle.

5. Thermodynamic evolution of atmosphere and upper ocean

This section examines how thermodynamic changes in the atmosphere and upper ocean manifest as cyclical increases and decreases in $\langle B \rangle_{\mathrm{DIB}}$, which are coupled to the cyclical amplification and decay of convection throughout D–R cycles. Figure 7 shows the bin-mean tendencies (color shading) of MSE, SST, and OHC integrated over different layers of the atmosphere and upper ocean. Note that color scales have been adjusted to account for the relative mass of each layer considered, so that similar colors represent similar tendencies of MSE or OHC within each layer of the atmosphere and ocean, respectively. Dry static energy tendencies (not shown) are small relative to MSE tendencies, which are dominated by moisture tendencies at all levels including the subcloud layer (950–1000 hPa).

First note that SST tendencies approaching $\pm$0.1 K day^{-1} are evident, with SST warming during periods characterized by more cumulus and congestus cloud types (Fig. 5, S1, T1, D1), and SST cooling during periods of enhanced MCS activity (Fig. 6, D3). SST tendencies approaching $\pm$0.1 K day^{-1} are notable, given the 2.5° $\times$ 2.5° scales being considered. The pattern of SST tendencies is closely matched by that of OHC tendencies, which are largely concentrated in the upper 50 m, and considerably larger in magnitude than MSE tendencies.

The deep convective D–R cycle can be characterized as follows. Enhanced cumulus cloudiness (Fig. 5, D1) is associated

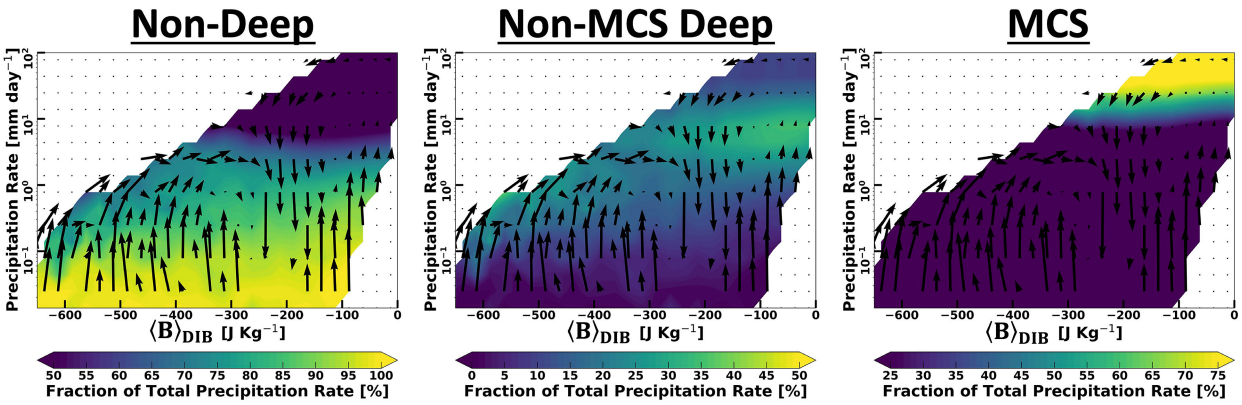

FIG. 6. As in Fig. 2b, except color shading shows MCS tracking estimates of the contribution of nondeep, non-MCS deep, and MCS precipitation types to total IMERG precipitation rate (Y axis). MCS tracking data are restricted to the time period of 2001–14, excluding years 2003–05, while vectors are calculated using IMERG precipitation and ERA5 thermodynamic fields from 2001 to 2015, as in Fig. 2b. All color scales have an equal dynamic range.

with warming SST and OHC, moistening of the boundary layer (1000–800 hPa), especially the subcloud layer, and drying of the lower and upper free troposphere (800–600 and 600–100 hPa, respectively). The transition from enhanced cumulus to congestus to narrow deep precipitation cloudiness (Fig. 5, D2) is associated with transitions from boundary layer moistening to drying, upper free troposphere drying to moistening, and OHC warming to cooling. Enhanced MCS activity (Fig. 6, D3) is associated with cooling SST and OHC, drying of the boundary layer, and moistening of the upper free troposphere. As MCS precipitation decreases, a mixed transitional cloud regime (Fig. 5, T2) is associated with a moistening boundary layer and drying upper free troposphere. Thermodynamic tendencies in T2 are likely to depend on antecedent conditions (i.e., transitions from S2 or D3), and must therefore be interpreted with caution.

The shallow convective D–R cycle can be characterized as follows. Enhanced cumulus (Fig. 5, S1) is associated with weakly warming or neutral SST and OHC, and drying of both the subcloud layer and lower free troposphere. As precipitation rates increase and stratocumulus clouds become enhanced (Fig. 5, S2), considerable moistening of the 950–800 hPa layer and lower free troposphere is evident, suggesting that the cumulus to stratocumulus transition is ventilating the subcloud layer. Interestingly, as $\langle B \rangle_{\mathrm{DIB}}$ increases into the mixed transitional cloud regime (T2), bin-mean precipitation rates decrease (downward vectors), the lower free troposphere transitions from moistening to drying, and the subcloud layer begins to moisten again. This is examined further below.

Figure 8 shows how the aforementioned thermodynamic tendencies impact $\langle B \rangle_{\mathrm{DIB}}$ and its constituent components. Variations in both $\langle B \rangle_{\mathrm{NOMIX}}$ and $\langle B \rangle_{\mathrm{MODENTRAIN}}$ make important contributions to variations in $\langle B \rangle_{\mathrm{DIB}}$. With the exception of conditions associated with enhanced MCS activity (Fig. 6, D3), the pattern of $\langle B \rangle_{\mathrm{NOMIX}}$ tendencies (Fig. 8) closely matches the pattern of subcloud-layer MSE tendencies (Fig. 7), indicating that $\langle B \rangle_{\mathrm{NOMIX}}$ variations are primarily driven by subcloud-layer moisture variations, and that day-to-day variations in lower-tropospheric static stability play little role in controlling day-to-day variations in $\langle B \rangle_{\mathrm{NOMIX}}$ during non-MCS conditions. The pattern of $\langle B \rangle_{\mathrm{MODENTRAIN}}$ (Fig. 8) reflects moisture variability in both the boundary layer and lower free troposphere (Fig. 7).

Enhanced cumulus in the shallow D–R cycle (S1) is associated with higher 800–600 hPa static stability (not shown) than enhanced cumulus in the deep D–R cycle (D1). Under these highly stable conditions (S1), bin-mean $\langle B \rangle_{\mathrm{NOMIX}}$ is near zero (appendix D, Fig. D1), indicating that even undiluted convective plumes would lack sufficient buoyancy to penetrate the freezing level. While the cumulus to stratocumulus transition moistens the 950–800 hPa layer and lower free troposphere (Fig. 7, S1, S2), drying of the subcloud layer drives further decreases in $\langle B \rangle_{\mathrm{NOMIX}}$ (Fig. 8, S1, S2). This drying of the subcloud layer and further decrease in $\langle B \rangle_{\mathrm{NOMIX}}$ may ultimately limit precipitation rates in the shallow D–R cycle, despite moistening (i.e., preconditioning) of the lower free troposphere by the cumulus to stratocumulus transition (S1 to S2).

In summary, moisture variability within the subcloud layer, overlying portions of the boundary layer, and the lower free troposphere all play important roles in determining day-to-day variations of $\langle B \rangle_{\mathrm{DIB}}$. Day-to-day variations in lower-tropospheric static stability play little role in controlling day-to-day variations in $\langle B \rangle_{\mathrm{DIB}}$ during non-MCS conditions. The following section will examine the processes driving variations in moisture and $\langle B \rangle_{\mathrm{DIB}}$.

6. Atmosphere–ocean coupled energy budgets of convective discharge–recharge cycles

a. *Motivation and formulation*

In the previous section, cyclical increases and decreases in $\langle B \rangle_{\mathrm{DIB}}$ were shown to result primarily from moisture variability in the boundary layer and lower free troposphere. To

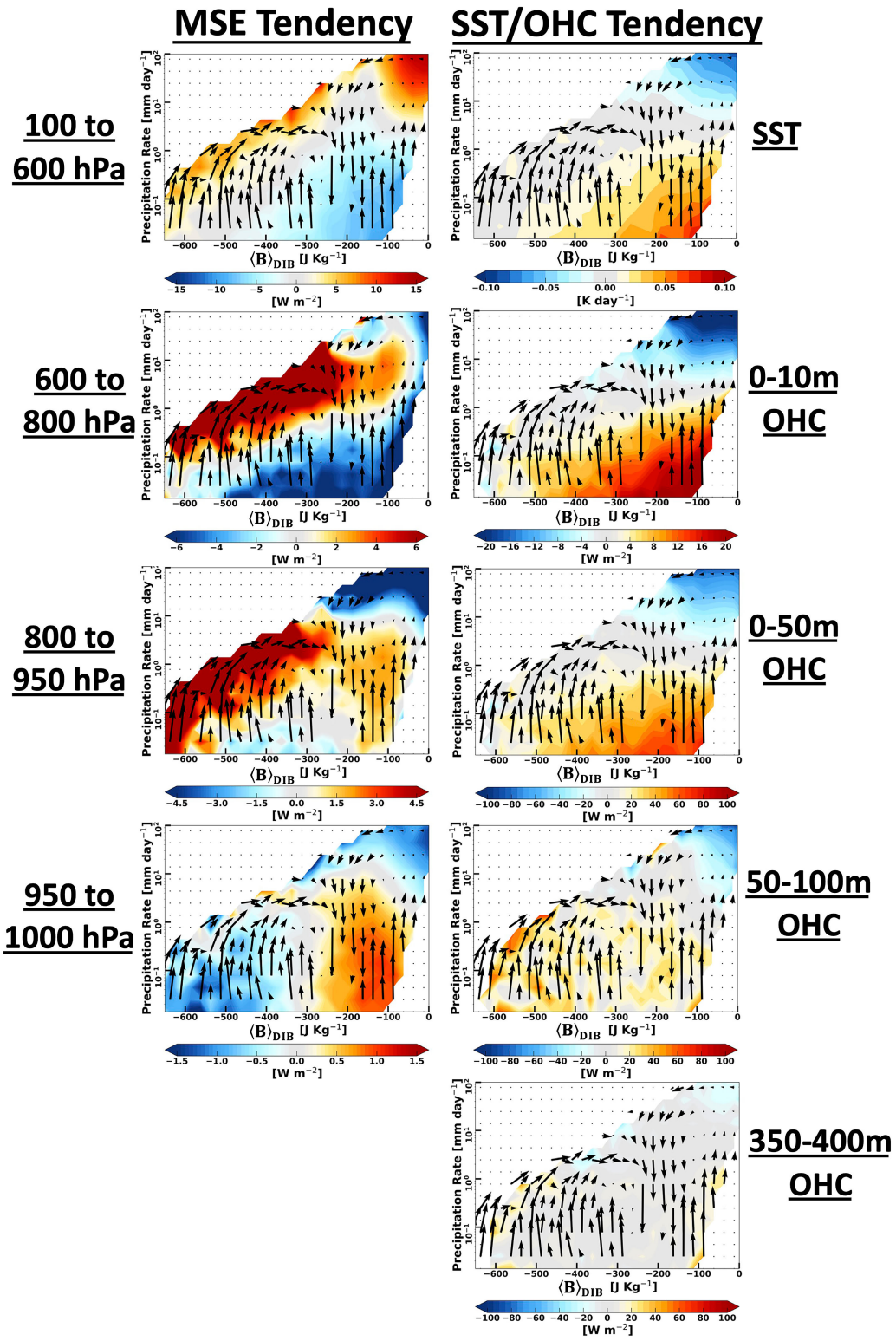

FIG. 7. As in Fig. 2b, except color shading shows bin-mean tendencies of moist static energy (MSE), SST, and ocean heat content (OHC) integrated over different layers of the atmosphere and upper ocean.

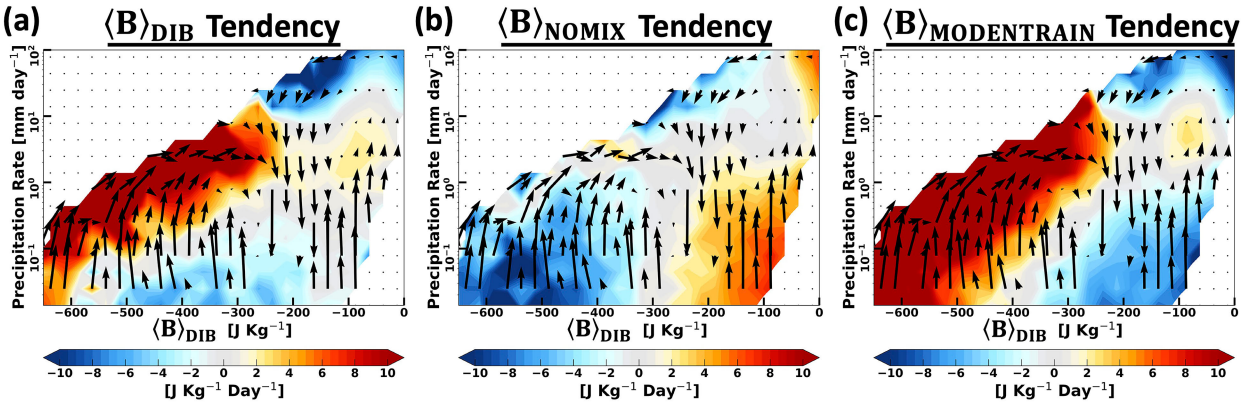

FIG. 8. As in Fig. 2b, except color shading shows bin-mean tendencies of $\langle B\rangle_{\mathrm{DIB}}$, $\langle B\rangle_{\mathrm{NOMIX}}$, and $\langle B\rangle_{\mathrm{MODENTRAIN}}$.

examine the processes driving this moisture variability, first consider the column integrated MSE budget. Assuming tropical WTG balance allows moisture variability to be related to MSE variability, and the processes (including diabatic) driving this variability (Sobel et al. 2001; Raymond 2001; Maloney 2009; Chikira 2014; Inoue et al. 2020; Adames and Maloney 2021), such that

$$L_v\left\langle\frac{\partial\overline{q}}{\partial t}\right\rangle \approx \left\langle\frac{\partial\overline{h}}{\partial t}\right\rangle = \underbrace{-\langle\overline{\mathbf{V}}\cdot\nabla\overline{h}\rangle - \left\langle\overline{\omega}\frac{\partial\overline{h}}{\partial p}\right\rangle}_{\text{Atmospheric Transport}} + \underbrace{E+H}_{\text{Surface Fluxes}} + \underbrace{\langle Q_r\rangle}_{\text{Radiation}}, \quad (5)$$

where L_v is the latent heat of vaporization, h is MSE, $\mathbf{V}$ and ω are the horizontal and vertical winds, E is evaporation, H is surface sensible heat flux, Q_r is radiative heating, overbars represent large-scale averages, and angle brackets represent vertical integrals from the surface to 100 hPa. Underbraces indicate the terms hereafter referred to as transport, surface fluxes, and radiation, respectively, and unresolved horizontal eddy transports have been neglected. The mean and seasonal cycle (first three harmonics) have been removed from these and all subsequent budget terms, which therefore represent variations from the slowly varying background state. The radiation term can be further expanded as

$$\langle Q_r\rangle = \mathrm{LW}|_{\mathrm{surface}} - \mathrm{LW}|_{\mathrm{100hPa}} + \mathrm{SW}|_{\mathrm{surface}} - \mathrm{SW}|_{\mathrm{100hPa}}, \quad (6)$$

where LW and SW are the net longwave and shortwave components, respectively, defined positive upward.

Initial examination of the MSE budget (Fig. 9) shows that surface fluxes (dominated by E) are playing a first-order role in both D–R cycles, indicating that the ocean is acting as an important anomalous source/sink of MSE, and should therefore be examined. As OHC variability is concentrated in the 0–50 m depth (Fig. 7), an OHC budget for this layer is examined. Similar to the atmospheric MSE budget, the 0–50 m OHC tendency results from transport, surface flux, and radiation processes, as given by

$$\left\langle\frac{\partial\overline{\mathrm{OHC}}}{\partial t}\right\rangle = \overbrace{-\langle\overline{\mathbf{V}}\cdot\nabla\overline{\mathrm{OHC}}\rangle - \left\langle\overline{w}\frac{\partial\overline{\mathrm{OHC}}}{\partial z}\right\rangle - A_h\nabla^2\mathrm{OHC} - \frac{A_z}{D}\frac{\partial\overline{\mathrm{OHC}}}{\partial z}}^{\text{Oceanic Transport}} \underbrace{-L_vE - H}_{\text{Surface Fluxes}} \underbrace{-\mathrm{LW}|_{\mathrm{surface}} - \mathrm{SW}_{\mathrm{surface}} + \mathrm{SW}_D}_{\text{Radiation}}, \quad (7)$$

where $\mathbf{V}$ and w are the horizontal and vertical currents, A_h and A_z are the horizontal and vertical eddy diffusivities, and D is the 50 m depth. The third and fourth transport terms are horizontal and vertical diffusion of OHC, respectively, and the final radiation term is penetrative shortwave, which is negligible at 50 m with respect to these budgets. The OHC budget terms are shown in Fig. 9 and discussed below.

The MSE and upper OHC budgets share units (W m^{-2}), surface flux terms, and surface radiation terms, and can therefore be combined to form an atmosphere–ocean coupled energy budget (Fig. 9) (Rydbeck et al. 2023), given by

$$\left\langle\frac{\partial\overline{c}}{\partial t}\right\rangle = \overbrace{-\langle\overline{\mathbf{V}}\cdot\nabla\overline{h}\rangle - \left\langle\overline{\omega}\frac{\partial\overline{h}}{\partial p}\right\rangle}^{\text{Atmospheric Transport}} \overbrace{-\langle\overline{\mathbf{V}}\cdot\nabla\overline{\mathrm{OHC}}\rangle - \left\langle\overline{w}\frac{\partial\overline{\mathrm{OHC}}}{\partial z}\right\rangle - A_h\nabla^2\mathrm{OHC} - \frac{A_z}{D}\frac{\partial\overline{\mathrm{OHC}}}{\partial z}}^{\text{Oceanic Transport}} \underbrace{-\mathrm{LW}|_{\mathrm{100hPa}} - \mathrm{SW}|_{\mathrm{100hPa}} + \mathrm{SW}|_D}_{\text{Radiation}}, \quad (8)$$

where $c \equiv h + \mathrm{OHC}$ is what we refer to here as the atmosphere–ocean coupled static energy (CSE). As radiative, sensible, and latent heat fluxes between the ocean and atmosphere do not impact CSE, changes in CSE result exclusively from energy transports by atmospheric and oceanic motions,

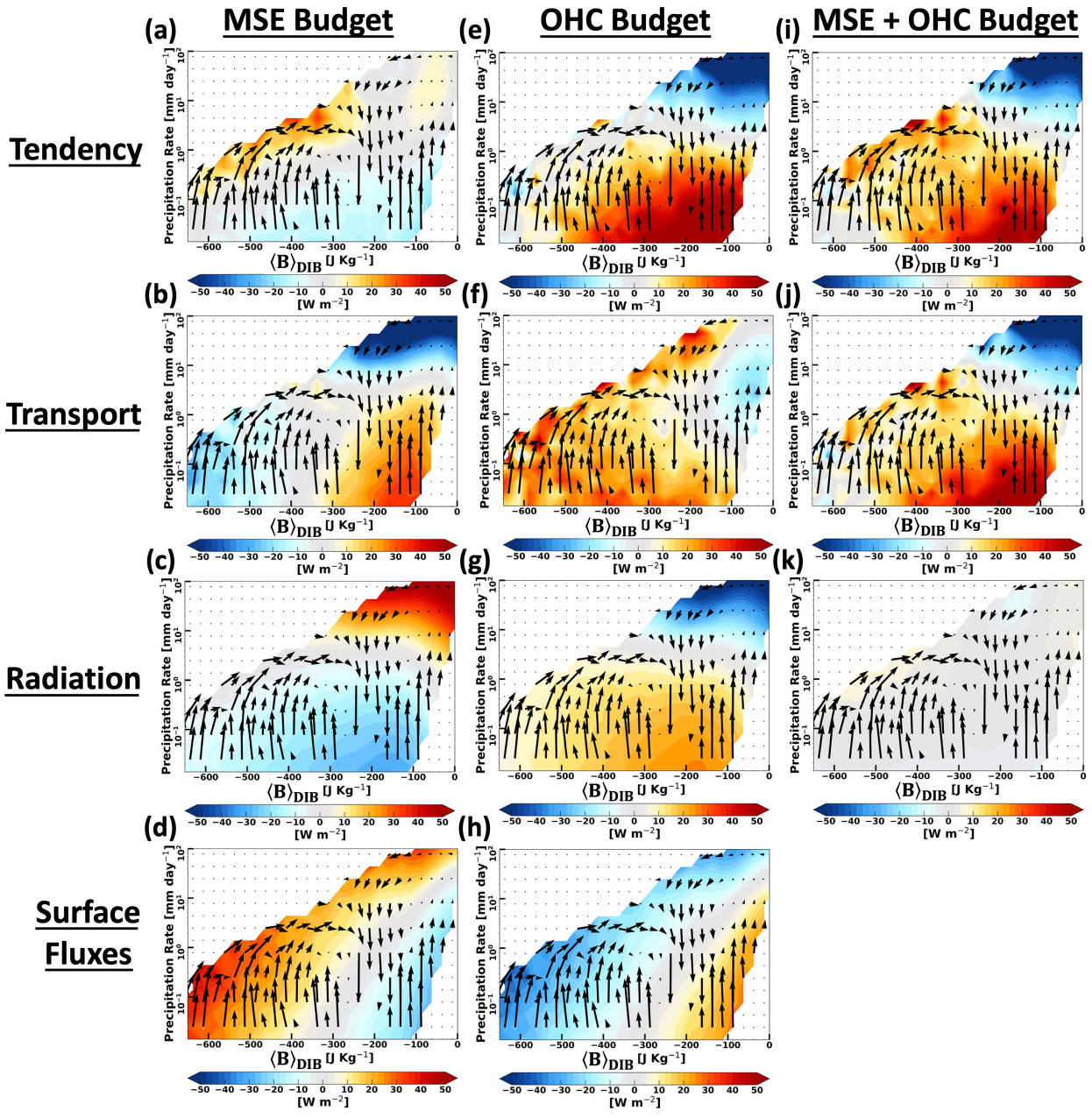

FIG. 9. As in Fig. 2b, except color shading shows MSE, 0–50 m OHC, and combined MSE–OHC budget terms described in Eqs. (5), (7), and (8), respectively.

net radiative fluxes at 100 hPa, and penetrative SW at 50 m, which again is negligible. With a suitable budget framework in place, the processes driving D–R cycles can now be examined.

b. *General examination*

Before examining each D–R cycle in detail, a general examination of the atmosphere–ocean coupled energy budget is warranted. Processes impacting MSE (Figs. 9b–d) are comparable in magnitude to those impacting OHC (Figs. 9f–h), but the former are considerably more balanced, resulting in relatively small net MSE tendencies (Fig. 9a). This is likely a result of WTG balance, which intimately links diabatic processes occurring in the atmosphere to atmospheric motions and attendant energy transports (Schumacher et al. 2004; Back and Bretherton 2009; Chikira 2014; Inoue et al. 2020). Atmospheric radiative feedbacks (Fig. 9c), which are dominated by the LW component, are almost completely offset by upper ocean radiative feedbacks (Fig. 9g), which are dominated by the SW component, resulting in near zero net radiative tendencies (Hartmann et al. 2001). Increases and decreases in atmosphere–ocean CSE

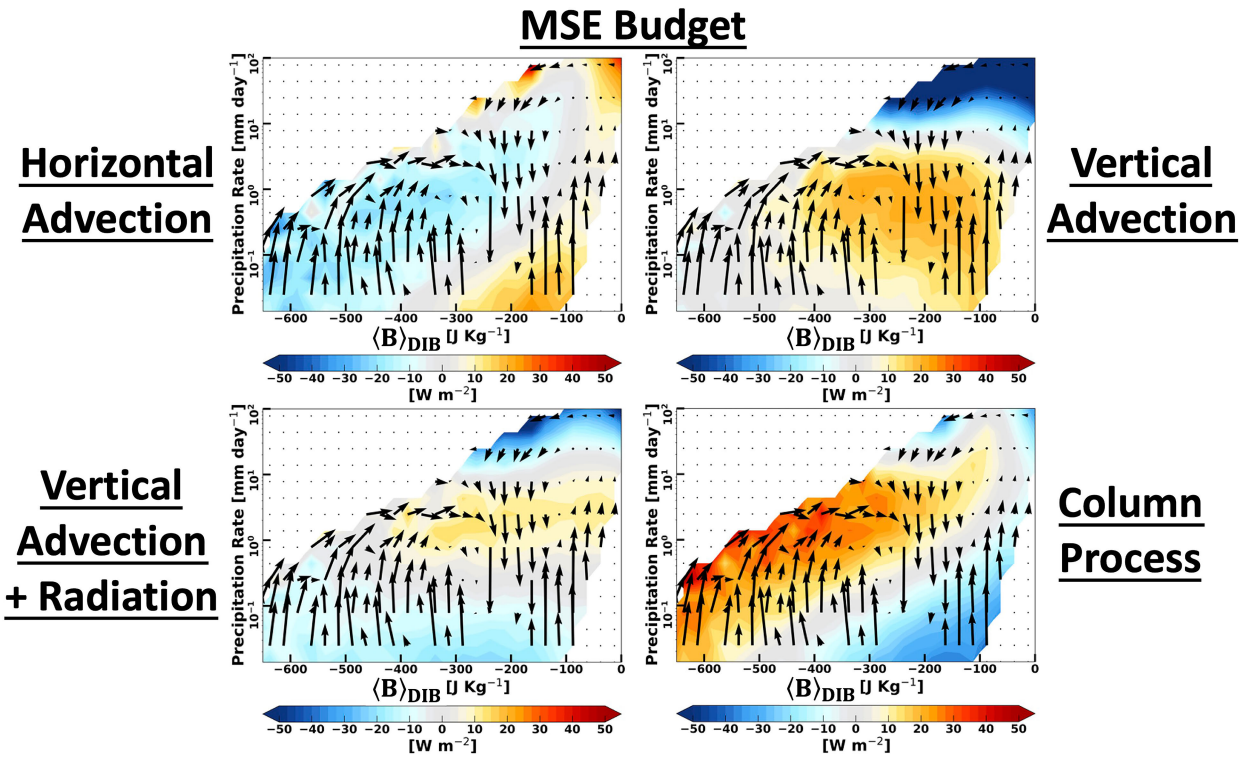

FIG. 10. As in Fig. 9, except color shading shows ERA5 MSE advective terms, the sum of vertical advection and radiation terms, and the column process. The column process is the sum of vertical MSE advection, radiation terms, and surface flux terms.

(Fig. 9i) are largely the result of atmospheric and oceanic transports processes (Figs. 9b,j, the latter typically associated with slower adjustment time scales and longer memory), but primarily realized as changes in OHC (Figs. 9e,i). CSE generally increases when $P < 1$ mm day^{-1}, and decreases when $P > 1$ mm day^{-1} (Fig. 9i).

c. *Energy budget of deep convective D–R cycle*

The deep convective D–R cycle can be characterized as follows. Enhanced cumulus cloudiness (Fig. 5, D1) is associated with MSE import by atmospheric transport processes (Fig. 9b), which results from both horizontal and vertical advection (Fig. 10), and is realized as a moistening of the boundary layer (Fig. 7). MSE import by atmospheric transport processes is opposed by enhanced LW radiative cooling (Fig. 9c) and reduced surface fluxes (Fig. 9d), resulting in a negative MSE tendency (Fig. 9a) and decreasing CSF (Fig. 3c), which is concentrated in the lower free troposphere (Fig. 7). Despite free tropospheric drying, bin-mean precipitation rates are increasing (upward vectors), indicating that increasing boundary layer MSE (Fig. 7) is providing sufficient $\langle B \rangle_{\mathrm{NOMIX}}$ (Fig. 8) to support the deepening of convection (Fig. 5, CG). Oceanic transport processes (Fig. 9f, D1), increased SW radiative heating (Fig. 9g), and reduced ocean-to-atmosphere surface fluxes (Fig. 9h, warm colors) all contribute to increasing OHC under these conditions (Fig. 9e), which exceeds the negative MSE tendency, resulting in a strong net positive CSE tendency (Fig. 9i).

The transition from enhanced cumulus to congestus to narrow deep precipitation cloudiness (Fig. 5, D2) is associated with sign changes in most of the MSE and OHC budget terms. As precipitation rates increase beyond 10 mm day^{-1} and MCS activity becomes widespread (Fig. 6, D3), atmospheric transports begin rapidly exporting MSE (Fig. 9b), with large-scale vertical advection (Fig. 10) drying the boundary layer (Fig. 7). This MSE export is countered by positive radiative feedbacks (Fig. 9c, reduced LW cooling) and enhanced surface fluxes (Fig. 9d) to such a degree that the overall MSE tendency (Fig. 9a) remains near zero or slightly positive. When considered from the perspective of the atmosphere alone, this near zero MSE tendency gives the perception that widespread MCS activity is associated with approximate energy balance. Yet OHC is rapidly decreasing (Fig. 9e) under these conditions, a result of greatly reduced incoming SW radiation (Fig. 9g) and enhanced conversion of OHC to MSE via enhanced ocean-to-atmosphere surface fluxes (Fig. 9h). When the atmosphere and ocean are considered together (Fig. 9i), a strong net negative CSE tendency results. As MCS precipitation decreases, the mixed transitional cloud regime (Fig. 5, T2) is associated with sign changes in most of the MSE and OHC budget terms, though again this regime must be interpreted with caution.

d. *Energy budget of shallow convective D–R cycle*

Throughout shallow convective D–R cycles, oceanic transport processes (Fig. 9f, S1, S2, T2, T1) and increased SW

radiative heating (Fig. 9g) are acting to increase OHC, which is converted to MSE and transferred to the atmosphere via enhanced surface fluxes (Fig. 9h), especially during the cumulus to stratocumulus transition (Fig. 5, S1, S2). When the atmosphere and ocean are considered together (Fig. 9i), CSE is steadily increasing throughout shallow convective D–R cycles.

During periods characterized by a mix of cumulus and cirrus cloud types (Fig. 5, S1), considerably enhanced surface fluxes (Fig. 9d) are opposed by enhanced LW cooling (Fig. 9c) and MSE export by atmospheric transports (Fig. 9b), resulting in near zero tendencies of MSE (Fig. 9a). As both $\langle B\rangle_{\mathrm{DIB}}$ and precipitation increase, and stratocumulus and congestus clouds become more prevalent (Figs. 5 and C1, S2), surface fluxes remain enhanced (Fig. 9d), but MSE transports (Fig. 9b) and radiative feedbacks (Fig. 9c) become less negative, resulting in a net positive MSE tendency (Fig. 9a). Examination of Fig. 10, which shows the "column process" terms (i.e., net effect of vertical advection, radiation, and surface fluxes; Chikira 2014), indicates that, in the absence of anomalous horizontal advective MSE export, convection may self-amplify by driving increases in MSE. The column process terms appear to encourage the transition from the shallow convective D–R cycle to the deep convective D–R cycle (S2 to T2 to D2). At precipitation rates between 1 and 10 mm day^{-1}, when non-MCS deep precipitation is more prevalent (Fig. 6), the net effect of vertical MSE advection and radiation is to drive a moderate increase in MSE (Fig. 10). This again suggests that, in the absence of anomalous horizontal drying, convection may self-amplify and transition from the shallow to deep convective D–R cycle. Under these conditions, MSE export by horizontal advection is the primary processes restraining convection from self-amplifying (Fig. 10).

7. Preliminary examination of DYNAMO field campaign

This section provides a preliminary examination of the DYNAMO field campaign, using this case study to illustrate results of previous sections, frame concepts discussed in section 8, and highlight their potential relevance to CCEWs and the MJO (Johnson and Ciesielski 2013; Chen et al. 2015; Johnson and Ciesielski 2017; Zhang and Yoneyama 2017). The DYNAMO field campaign's NSA experienced three consecutive periods of enhanced convection (Fig. 11), each preceded by a period of suppressed convection. Following the end of period 3, which coincides with the end of the CSU V3 DYNAMO dataset, a fourth period of suppressed convection persisted throughout January 2012.

Considerable day-to-day variability in precipitation occurred within the first three periods. While NSA daily averaged $\langle B\rangle_{\mathrm{DIB}}$ remained above -200 J kg^{-1} throughout the majority of the first three periods, a dramatic decrease in both $\langle B\rangle_{\mathrm{DIB}}$ and precipitation rate occurred near the end of the third period. Satellite imagery indicates that widespread deep convective activity was occurring over the NSA on 21 December, the day of maximum period 3 precipitation. Following this widespread deep convective activity, $\langle B\rangle_{\mathrm{DIB}}$ and precipitation continuously decreased until 28 December (purple square), when cloudiness over the NSA was characterized by a mix of shallow cumulus and upper-level cirrus. On 31 December (purple triangle), the final day of the CSU V3 DYNAMO dataset, precipitation and $\langle B\rangle_{\mathrm{DIB}}$ had increased from previous days, and more expansive shallow cumulus features are visible over the NSA. This progression of cloud types is consistent with the analysis presented in section 4. Following the dramatic "discharge" of $\langle B\rangle_{\mathrm{DIB}}$ at the end of December 2011, $\langle B\rangle_{\mathrm{DIB}}$ remained below -200 J kg^{-1} and precipitation remained suppressed throughout all of January 2012.

NSA mean MSE was anomalously high (Fig. 12, red line) during periods of enhanced precipitation (Fig. 12, black line), and neutral or anomalously low during periods of suppressed precipitation, varying by approximately $\pm 0.25 \times 10^8$ J m^{-2} (Sobel et al. 2014; Ruppert and Johnson 2015). NSA mean 0–50 m OHC (Fig. 12, blue line) was anomalously high prior to each of the three periods of enhanced precipitation, and decreased rapidly during, and immediately following, each period of enhanced precipitation. These decreases in OHC were $\sim$1–1.5 $\times$ 10^8 J m^{-2}, several times larger than variations in NSA MSE, consistent with the analysis presented in section 6. Following each period of enhanced precipitation, OHC rapidly recovered during periods of suppressed precipitation. While OHC completely recovered following period 1, OHC only partially recovered following periods 2 and 3, decreasing by $\sim 2 \times 10^8$ J m^{-2} between mid-November and late December. 0–50 m OHC, which was anomalous high throughout nearly all of the three successive periods of enhanced convection, was anomalously low by the end of period 3, coincident with the onset of persistent suppressed convective conditions. While both MSE and OHC partially recovered following the third period of enhanced precipitation, OHC remained near neutral throughout January, while MSE remained anomalously low.

8. Discussion

a. *Balance, imbalance, and discharge–recharge cycles*

Results of the atmosphere–ocean coupled energy budget (Fig. 9) are largely consistent with previous multiple-equilibria studies of tropical convection (Sobel et al. 2007; Raymond et al. 2009; Sessions et al. 2010), but emphasize the central role that the upper ocean plays in determining viable states of balance. While MSE balance occurs under a variety of conditions in both the shallow and deep convective D–R cycles, many of these conditions are characterized by rapidly changing upper OHC and CSE imbalance (Fig. 9), highlighting that MSE balance does not necessarily imply conditions of equilibrium, stasis, or sustainability (appendix A). The multiple equilibria model described by Raymond et al. (2009), and derived in appendix A, assumes that feedbacks arising from perturbations in transport processes, surface fluxes, and radiation can be neglected when determining the evolution of convection when not in an equilibrium state. Findings of this study suggest that each of these feedbacks play important roles in driving the cyclical amplification and decay of convection in D–R cycles, and may play important roles in driving transitions between shallow and deep convective D–R cycles.

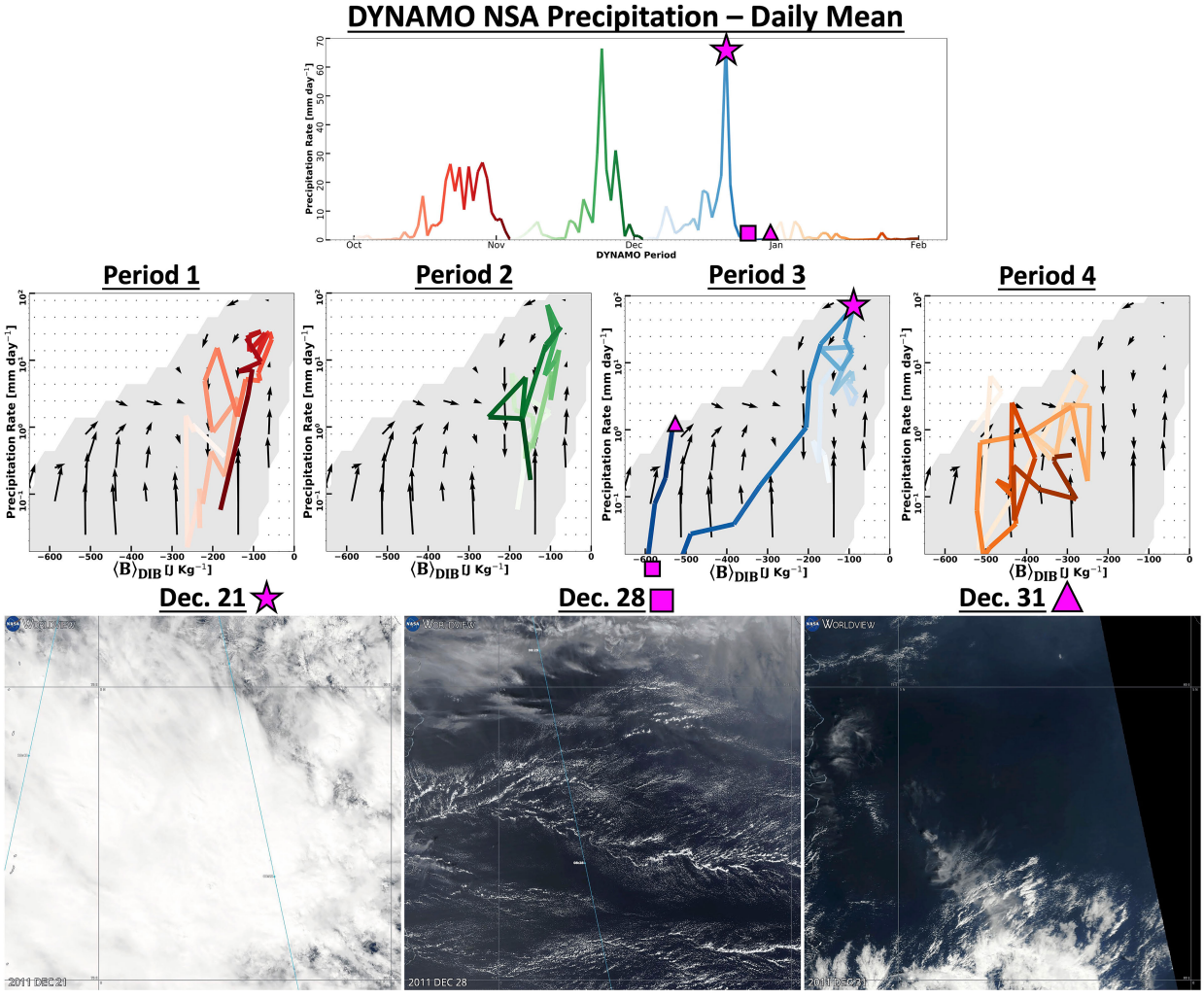

FIG. 11. (top) DYNAMO NSA average daily mean precipitation, with red, green, blue, and orange colored lines corresponding to periods 1–4, respectively. The magenta star, square, and triangle indicate 21, 28, and 31 Dec 2011, respectively, and are repeated in other rows. (middle) Temporal coevolution of NSA average precipitation rate and $\langle B \rangle_{\mathrm{DIB}}$, with color shading corresponding to the four time periods shown in the top row. Vectors are as in Fig. 2b, calculated using IMERG precipitation and ERA5 thermodynamic fields from 2001 to 2015. $P < 10^{-2}$ mm day^{-1} on 28 Dec; therefore, the magenta square is plotted off the bottom of the period 3 panel. (bottom) NASA Worldview imagery approximately corresponding to the NSA domain for select days from period 3, as indicated by the magenta shapes. In all cases, CSU V3b data were used for 1 Oct to 31 Dec 2011 (periods 1–3), and NSA average IMERG precipitation and ERA5 $\langle B \rangle_{\mathrm{DIB}}$ were used for January 2012 (period 4).

In the absence of anomalous horizontal advective drying, positive column process feedbacks occurring during cumulus–stratocumulus–congestus deepening may drive transitions from the shallow to deep convective D–R cycles (Fig. 9, S1 to S2 to T2 to D2) (Yano and Plant 2012b; Inoue et al. 2021). The mature and decaying phases of MCSs drive considerable "discharge" of upper OHC and $\langle B \rangle_{\mathrm{DIB}}$, suggesting that MCSs can, at times, contribute to transitions from the deep to shallow convective D–R cycle (Figs. 9 and 3, respectively, D3 to T2 to T1 to S1). The large amount of upper-level cirrus clouds observed during the shallow convective D–R cycle, which is otherwise characterized predominantly by shallow cumulus and stratocumulus cloud types that do not extend above the freezing level, also suggests that these suppressed convective conditions are frequently preceded by widespread deep convection. The deep to shallow convective D–R cycle transition near the end of period 3 of the DYNAMO case study provides anecdotal support for this supposition, which is further supported by supplemental analysis in appendix B. The discharge of OHC that occurs during the deep-to-shallow D–R transition, followed by the slow warming of the upper ocean and enhanced surface fluxes occurring during the cyclical transitions between cumulus and stratocumulus (S1, S2), is reminiscent of the conditions associated with warming–deepening decoupling of cloud-topped boundary layers (Bretherton and Wyant 1997; Wood and Bretherton 2004). Recall that the

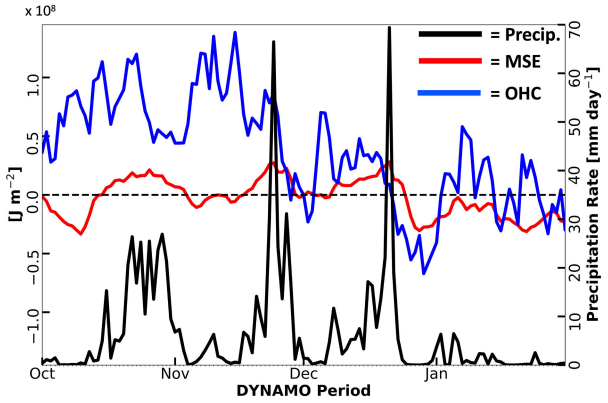

FIG. 12. DYNAMO NSA average daily mean precipitation (black line), ERA5 MSE anomaly (red line), and 0–50 m HYCOM OHC anomaly (blue line) for 1 Oct 2011–31 Jan 2012. MSE and OHC anomalies are calculated as described in section 2a.

evolution of $\langle B \rangle_{\mathrm{DIB}}$ and precipitation often departs from the conditional-mean trajectories discussed in previous sections (Fig. 3), highlighting the considerable role that processes such as tropical–extratropical interactions and equatorial wave dynamics in the atmosphere and ocean may play in driving transitions between the shallow and deep convective D–R cycles.

The near perfect asymmetry between atmospheric LW and oceanic SW radiative feedbacks indicates that their net effect is to change the composition of atmosphere–ocean CSE (i.e., MSE versus OHC) without changing the total quantity of CSE, similar to surface flux feedbacks (Hartmann et al. 2001; Tobin et al. 2012). While reduced LW radiative cooling of the atmosphere provides an important positive feedback to deep convection, the associated reduction of SW absorption by the upper ocean and cooling of SST/OHC may limit the duration for which enhanced ocean-to-atmosphere surface fluxes can be sustained, providing a negative, though likely delayed, feedback to deep convection. OHC may therefore limit the ability of radiative and surface flux feedbacks to support extended or successive periods of enhanced convection. The DYNAMO case study further indicates that $\langle B \rangle_{\mathrm{DIB}}$ and 0–50 m OHC anomalies, when considered together, may prove useful in understanding and predicting successive versus terminating MJO events (Matthews 2008; Straub 2013; Maloney and Wolding 2015; Stachnik et al. 2015; Chrisler and Stachnik 2021).

MCSs appear to be unique in their ability to rapidly discharge upper OHC (Fig. 9e, D3), which is recharged when the clouds ensemble is composed mainly of cumulus, stratocumulus, and congestus cloud types (Fig. 5), and precipitation is "nondeep" (Fig. 6). Under suppressed convective conditions ($P < 1$ mm day^{-1}), recharge of OHC is much slower in the shallow convective D–R cycle than in the deep convective D–R cycle, largely as a result of enhanced surface flux feedbacks in the former (Fig. 9, S1 and D1, respectively). The presence of widespread cirrus clouds during relatively stable conditions (Fig. 5, S1) reducing shortwave radiative heating of the upper ocean (Fig. 9g, S1) may also be contributing to these differences.

b. *Organizational feedbacks and discharge–recharge cycles*

When considering day-to-day variations on horizontal scales of ~250 km × 250 km, conditionally averaged precipitation rate is a rapidly increasing function of $\langle B \rangle_{\mathrm{DIB}}$ (Fig. 2a), indicating that $\langle B \rangle_{\mathrm{DIB}}$ is a "relevant" measure of large-scale average convective instability. Yet there is considerable variability about this conditional mean relationship, with precipitation rates varying by roughly two orders of magnitude for any fixed value of $\langle B \rangle_{\mathrm{DIB}}$ (Fig. 2b). Such variability in the $\langle B \rangle_{\mathrm{DIB}}$–precipitation relationship may result from $\langle B \rangle_{\mathrm{DIB}}$ being an imperfect or incomplete measure of large-scale average convective instability. While this is undoubtedly true, many studies argue that no measure of large-scale average convective instability can reflect the capacity of the atmosphere to support convective activity without accounting for organizational feedbacks (Donner 1993; Kingsmill and Houze 1999; Park 2014; Mapes and Neale 2011; Moncrieff et al. 2017; Bengtsson et al. 2021; Shamekh et al. 2023).

In this study, "organizational feedbacks" refer specifically to "structures, relationships, and processes with functional roles (i.e., systematic or net impacts on larger scales)" occurring on the mesoscale or smaller, which can be understood as "non-randomness in meteorological fields in convecting regions" (Mapes and Neale 2011; Moncrieff 2004). Organizational feedbacks are conspicuous in real-world convection, and a recent observational study by Bony et al. (2020b) found deep convection to be "highly clustered" and nonrandomly distributed across the tropics (Mapes 1993; Kingsmill and Houze 1999; Houze 2004). To illustrate how numerous and varied organizational feedbacks are, consider the following observationally based examples. Convective downdrafts reduce large-scale mean boundary layer moist enthalpy, but provide the "triggering energy" (e.g., gust fronts) needed for adjacent air with relatively high moist enthalpy to rise and overcome CIN (Mapes 2000). Convection organized along outflow boundaries may rise through an environment "preconditioned" by moisture detrained from antecedent convection, promoting its further development and deepening. Deep convective clouds in close proximity can aggregate into MCSs, which induce circulations on scales larger than those of the individual up- and downdrafts (Moncrieff 2004; Houze 2018). Gravity waves propagating away from MCSs induce low-level convergence in regions adjacent to the MCS, making those regions more favorable for subsequent convection, and further contributing to the "gregariousness" of tropical convection (Mapes 1993).

Mapes and Neale (2011) suggested that "since buoyant ascent involves natural selection, subgrid structure makes convection systematically deeper and stronger than the pure unorganized case: plumes of average (or randomly sampled) air rising in the average environment." Angulo-Umana and Kim (2023) provided observational evidence of precipitation enhancement due to mesoscale convective clustering (PEMC), showing that for scenes with the same CSF and convective area fraction, strongly clustered oceanic convection precipitated more intensely than weakly clustered convection. Using global storm-resolving simulations, Shamekh et al. (2023) showed that

while a neural network trained on large-scale average thermodynamic quantities greatly underestimated predicted precipitation variability and extremes, a similar neural network that included a measure of smaller-scale organization correctly predicted these quantities.

The deep convective D–R cycle is characterized by considerable changes in mesoscale convective organization and, for any fixed value of $\langle B \rangle_{\mathrm{DIB}}$ within this D–R cycle, higher precipitation rates are associated with more organized deep convection, while lower precipitation rates are associated with less organized deep convection (Fig. 6). This suggests that organizational feedbacks such as PEMC are allowing highly organized deep convection to flourish in large-scale average thermodynamic environments that would otherwise be unfavorable for less organized convection. The counterclockwise coevolution of $\langle B \rangle_{\mathrm{DIB}}$ and precipitation rate (Fig. 6, vectors) indicates that organizational feedbacks are helping sustain MCS activity while $\langle B \rangle_{\mathrm{DIB}}$ and CSE (Figs. 3b and 9i, respectively) are discharged below levels required to support less organized convection, effectively "overspending" convective instability. Once $\langle B \rangle_{\mathrm{DIB}}$ and CSE are discharged to levels where not even highly organized convection can be supported, convection decays (downward vectors) and remains relatively quiescent while $\langle B \rangle_{\mathrm{NOMIX}}$ and CSE are recharged (Figs. 8 and 9i, respectively, warm colors) to the higher levels required for less organized convection to reinitiate, amplify (upward vectors), and reorganize upscale. This organizationally driven discharge–recharge deficit may be approximated as the difference between the "critical point" of organized and disorganized convection, $\langle B \rangle_{\mathrm{DIBcrit,org}} - \langle B \rangle_{\mathrm{DIBcrit,disorg}}$ (Peters and Neelin 2006; Neelin et al. 2009; Ahmed et al. 2020). Mesoscale convective organization is poorly represented in many current weather and climate models. In the absence of an organizationally driven discharge–recharge deficit of large-scale convective instability, convection could be more easily maintained near a state of quasi equilibrium, contributing to both a lack of convective variability and too frequent light to moderate precipitation, as has been documented in many models (Stephens et al. 2010).

Predominantly shallow cloud populations producing less than 1 mm day^{-1} are associated with dramatically different subcloud-layer MSE tendencies (Fig. 7), MSE transports, radiative feedbacks, and surface flux feedbacks (Figs. 9b–d), depending on if those cloud populations are occurring in relatively stable or unstable environments (S1 and D1, respectively). Lower-tropospheric static stability, which is greater in S1 than D1, is a known large-scale control of shallow convection organization (e.g., Bony et al. 2020a). Additional characterization of organizational changes in the shallow cloud population is a focus of ongoing work.

c. *Framework for identification and examination of D–R cycles*

Several approaches have been used to identify and examine D–R cycles, including gross moist stability (GMS) plane analysis (Inoue and Back 2017; Inoue et al. 2021; Maithel and Back 2022), examination of the temporal coevolution of precipitation and various measures of the thermodynamic environment (Wolding et al. 2020a; Yano et al. 2020; Chen et al. 2022), and assessments of the evolution of vertical moisture and/or temperature stratification (Igel 2017; Wolding et al. 2022), among others (Masunaga and L'Ecuyer 2014; Hannah et al. 2016). Each approach has respective advantages and disadvantages, and provides a different perspective of D–R cycles. For example, GMS plane analysis clearly distinguishes amplifying and decaying convective conditions, but requires knowledge of dynamic and thermodynamic fields where only limited or poorly resolved direct observations are available (e.g., large-scale vertical velocity, vertical MSE gradient) (Inoue and Back 2017; Inoue et al. 2021; Maithel and Back 2022). Examination of the temporal coevolution of precipitation and CSF leverages more directly observed fields, but neglects variability in the vertical structure of both moisture and temperature, which have been shown to substantially influence convective variability (Raymond et al. 2003; Khouider and Majda 2006; Holloway and Neelin 2009; Tulich and Mapes 2010; Kuang 2010; Sahany et al. 2012; Powell 2019; Fuchs-Stone et al. 2020; Wolding et al. 2020b; Raymond and Fuchs-Stone 2021). Consideration of the vertical structure of thermodynamic variability may provide a more sophisticated assessment of convective instability, if well observed. Unfortunately, infrared and microwave sounders, which together help constrain column moisture variability at large scales, have coarse vertical resolution, allowing analysis systems to make compensating errors in the vertical structure of humidity that approximately preserve column integrated water vapor, and leaving the boundary layer particularly susceptible to systematic errors arising from parameterized processes (Poli et al. 2010; Xie et al. 2012; Pincus et al. 2017; Ho et al. 2020; Ren et al. 2021; Wolding et al. 2022; Sentić et al. 2022; Serra et al. 2023). Each of these approaches have numerous other strengths and weaknesses not mentioned here.

This study attempts to use a "best of both worlds" approach to examining convective D–R cycles, considering the vertical structure of thermodynamic variability when necessary, and leveraging the advantages of column integration of MSE and/or OHC when appropriate. In many respects, results of this study are consistent with those of previous studies. Using a GMS phase angle analysis, Maithel and Back (2022) identified both dry and moist equilibrium states. Using a two-layer measure of moisture stratification, Igel (2017) identified both shallow and deep convective D–R cycles. Using a GMS plane analysis, Inoue et al. (2021) showed that, in the absence of anomalous horizontal advective drying, the column process leads to self-amplification of convection. This study serves as a natural extension of prior D–R cycle research by more fully characterizing the evolution of the cloud population throughout D–R cycles, providing a more detailed analysis of thermodynamic tendencies in the atmosphere and ocean, and by examining both MSE and OHC budgets.

d. *Primary limitations and ongoing research*

Foremost among the many limitations of this study is the reliance on thermodynamic profiles from reanalysis, which are

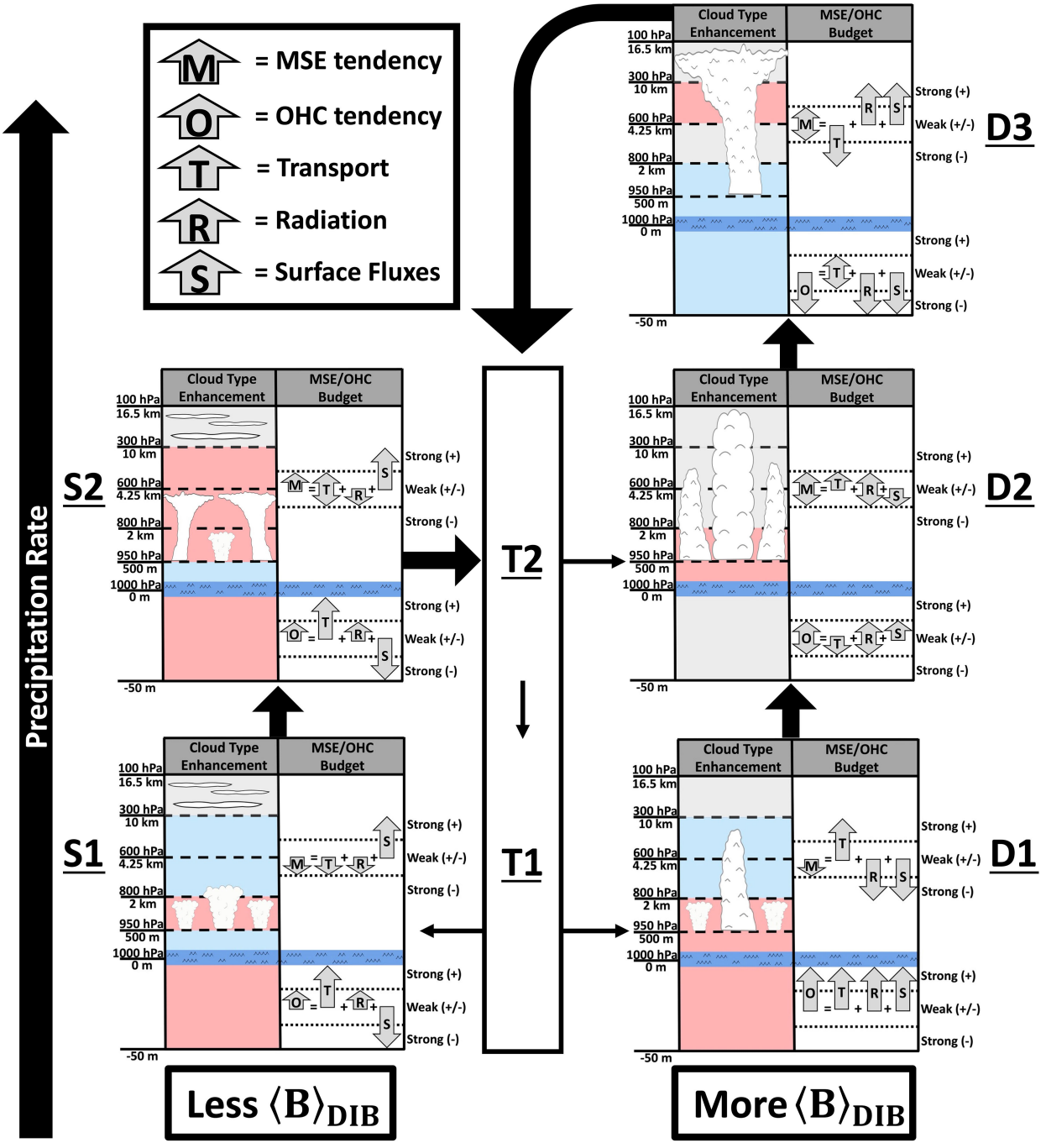

FIG. 13. Schematic summarizing cloud-type enhancement, MSE and OHC tendencies for various layers of the atmosphere and upper ocean (color shading; warm = positive, cool = negative), and MSE and OHC budgets for each regime (S1–D3) outlined in Fig. 4. A regime averaged value of 15 W m^{-2} delineates "strong" and "weak" budget processes.

known to have systematic and conditionally dependent biases (Pincus et al. 2017; Wolding et al. 2022; Serra et al. 2023). More sophisticated approaches are needed to understand the processes controlling horizontal MSE advection, which varies systematically throughout D–R cycles (Wang et al. 2016; Maithel and Back 2022). More explicit quantification of organizational feedbacks using metrics such as PEMC and the Iorg organization index, a focus of ongoing work, is needed to advance understanding of these processes and guide model development (Tompkins and Semie 2017; Bony et al. 2020b; Angulo-Umana and Kim 2023). The conditional mean analysis used to examine transitional regimes (T1, T2) does not distinguish between different antecedent conditions (e.g., transitions from S2 to T2 versus D3 to T2), which warrant further examination.

9. Summary and conclusions

The cyclical amplification and decay of convection is observed ubiquitously over tropical oceans, and arises from coupled feedbacks between clouds and their surrounding environment (Inoue and Back 2017; Inoue et al. 2021). In this study, shallow and deep convective "discharge–recharge cycles" (D–R cycles) are initially identified by examining day-to-day covariability between IMERG precipitation and ERA5 lower-tropospheric vertically integrated buoyancy ($\langle B \rangle_{\mathrm{DIB}}$) over the Indian and western Pacific Oceans. These D–R cycles are then further distinguished through analysis of thermodynamic tendencies of the atmosphere and ocean, and budgets of moist static energy (MSE) and upper ocean heat content (OHC). The primary findings of this study are summarized in Fig. 13, and discussed below.

The deep convective D–R cycle can be characterized as follows. Enhanced shallow cumulus cloudiness is associated with increasing OHC, moistening of the boundary layer, and drying of the free troposphere (Fig. 13, D1). Oceanic transport processes, SW radiative heating, and suppressed ocean-to-atmosphere surface fluxes all contribute to increasing OHC. Enhanced MSE import via atmospheric transport processes is opposed by enhanced longwave radiative cooling and suppressed surface fluxes, resulting in a net drying of the column. Despite this net drying, which is realized as a drying of the free troposphere, increasing boundary layer moisture is able to support the deepening of convection. The transition from enhanced cumulus to congestus to narrow deep precipitation is associated with sign changes in many of the MSE and OHC budget terms (Fig. 13, D2). As precipitation rates increase beyond 10 mm day^{-1}, enhanced mesoscale convective system (MCS) activity begins rapidly exporting MSE via large-scale vertical MSE advection, resulting in a drying of the boundary layer (Fig. 13, D3). This MSE export is supported by radiative and surface flux feedbacks, which act as anomalous sources of MSE at the expense of OHC, resulting in a neutral MSE tendency, but rapidly declining OHC. Decreasing MCS precipitation is associated with a mixed transitional cloud regime and sign changes in most of the MSE and OHC budget terms, though this regime must be interpreted with caution, and is therefore not described in detail (Fig. 13, T2, T1).

The shallow convective D–R cycle is characterized by alternating enhancements of cumulus and stratocumulus, in the presence of widespread upper-level cirrus (Fig. 13, S1, S2). Oceanic transport processes and increased SW heating drive a slow increase in OHC, despite the rapid conversion of OHC to MSE via enhanced surface fluxes, which are particularly strong in the cumulus and stratocumulus transition (S1 to S2). Despite these enhanced surface fluxes, anomalous drying of the subcloud layer occurs, with moistening limited to overlying portions of the boundary layer during periods of enhanced cumulus (S1), and deepening to include the free troposphere during periods of enhanced stratocumulus (S2).

The deepening of both moistening and convection in the cumulus to stratocumulus transition is associated with a positive column processes feedback which can, in the absence of anomalous horizontal advective drying, drive the self-amplification of convection, and the transition from the shallow to deep D–R cycle (S2 to T2 to D2). MCSs are unique in their ability to rapidly discharge both $\langle B \rangle_{\mathrm{DIB}}$ and OHC, and can, at times, drive the transition from the deep to shallow D–R cycle (D3 to T2 to T1 to S1), as seen anecdotally during the DYNAMO field campaign.

Examination of the atmosphere–ocean coupled energy budget provides more general insights to how day-to-day convective variability both impacts, and is impacted by, MSE and OHC variability. Feedbacks arising from atmospheric and oceanic transport processes, surface fluxes, and radiation all play important roles in driving the cyclical amplification and decay of convection in D–R cycles. Atmospheric LW and oceanic SW radiative feedbacks are of nearly equal magnitude but opposite sign (Hartmann et al. 2001), having the net effect of changing the composition of atmosphere–ocean coupled static energy (CSE = MSE + OHC) without changing the total quantity of CSE, similar to surface fluxes. Variability in the processes impacting MSE is comparable in magnitude to, but considerably more balanced than, variability in the processes impacting OHC. Variations in the quantity of CSE result primarily from atmospheric and oceanic transport processes, but are mainly realized as changes in OHC.

Atmosphere–ocean coupled energy budgets of convective D–R cycles may prove useful for guiding development of atmosphere–ocean coupled weather and climate models. Consideration of MSE *and* upper OHC may prove useful in understanding prolonged periods of suppressed convection, successive periods of enhanced convection, and perhaps even successive versus terminating MJO events.

Acknowledgments. Lead author Wolding extends his gratitude to Kathleen Schiro, Mark Miller, David Raymond, and Brian Mapes for conversations that improved this work. BW also thanks Ángel Adames, James Ruppert, and Walter Hannah for contributing clouds to the schematics. Thoughtful reviews by Larissa Back, Jun-Ichi Yano, and an anonymous reviewer greatly improved this manuscript. BW was partially supported by the California Department for Water Resources (CDWR). BW and ILM were partially supported by NOAA Cooperative Agreements NA17OAR4320101 and NA22OAR4320151. BW (AGS-2225957) and FA (AGS-2225956) were supported in part by NSF. Adam Rydbeck is supported by NRL base funding and ONR DRI Projects MISO-BoB and PISTON. ERD was supported by NASA CYGNSS Grant 80NSSC21K1004 and DOE Regional and Global Model Analysis DE-SC0020092.

Data availability statement. All data used in this study are publicly available. ERA5 data from the NCAR Research Data Archive (RDA) at https://rda.ucar.edu. HYCOM reanalysis data at https://www.hycom.org/dataserver/gofs-3pt0/reanalysis. The global merged infrared radiances and Integrated Multi-satellitE Retrievals precipitation data V06 from the National Aeronautics and Space Administration Goddard Earth Sciences Data and Information Services Center at https://doi.org/10.5067/P4HZB9N27EKU and https://doi.org/

10.5067/GPM/IMERG/3B-HH/06. *CloudSat* data at https://cloudsat.atmos.colostate.edu/data and processed EOs available from Riley Dellaripa and Mapes (2023). TRMM precipitation data at https://gpm.nasa.gov/data-access/downloads/trmm. CSU DYNAMO V3b NSA data at http://johnson.atmos.colostate.edu/dynamo/products/array_averages/index.html.

APPENDIX A

Normalized Gross Moist Stability–Dependent Multiple Equilibria Model

Building off of work by Raymond (2000), Raymond et al. (2009) describe how precipitation rate and CSF may evolve if the normalized gross moist stability (NGMS), a measure of how efficiently atmospheric transport processes [Eq. (5)] export MSE, increases as convective activity increases. This model is particularly relevant to the present study because it results in a bistable system, where a humid, enhanced convective equilibrium state is separated from a dry, suppressed convective equilibrium state by an unstable equilibrium state (Fig. A1), similar to results seen in sections 3 and 6. This appendix outlines the model and its associated assumptions, which is not formally derived elsewhere in published literature.

Column integrated budgets for specific humidity (q) and moist static energy (h) are given by

$$\left\langle \frac{\partial \overline{h}}{\partial t} \right\rangle = -\langle \overline{\mathbf{V}} \cdot \nabla \overline{h} \rangle - \left\langle \overline{\omega} \frac{\partial \overline{h}}{\partial p} \right\rangle + E + H + \langle Q_r \rangle, \tag{A1}$$

$$\left\langle \frac{\partial \overline{q}}{\partial t} \right\rangle = -\langle \overline{\mathbf{V}} \cdot \nabla \overline{q} \rangle - \left\langle \overline{\omega} \frac{\partial \overline{q}}{\partial p} \right\rangle + E - P, \tag{A2}$$

where E is evaporation, P is precipitation, H is surface sensible heat flux, and Q_r is radiative heating, and unresolved horizontal eddy transports have been neglected. Overbars represent large-scale averages, and angle brackets represent vertical integrals from the surface to 100 hPa. Multiplication of specific humidity q, evaporation E, and precipitation P by the latent heat L_v is implicit in Eq. (A2), which therefore shares units with Eq. (A1).

Here, NGMS is defined as

$$\Gamma = \frac{-\langle \overline{\mathbf{V}} \cdot \nabla \overline{h} \rangle - \left\langle \overline{\omega} \frac{\partial \overline{h}}{\partial p} \right\rangle}{\langle \overline{\mathbf{V}} \cdot \nabla \overline{q} \rangle + \left\langle \overline{\omega} \frac{\partial \overline{q}}{\partial p} \right\rangle}. \tag{A3}$$

Assuming WTG balance, Eq. (A1) becomes

$$\left\langle \frac{\partial \overline{q}}{\partial t} \right\rangle = -\langle \overline{\mathbf{V}} \cdot \nabla \overline{h} \rangle - \left\langle \overline{\omega} \frac{\partial \overline{h}}{\partial p} \right\rangle + E + H + \langle Q_r \rangle. \tag{A4}$$

Next it is *assumed* that precipitation tendency is proportional to column moisture tendency, such that

$$\left\langle \frac{\partial \overline{q}}{\partial t} \right\rangle = \frac{1}{\alpha} \frac{\partial P}{\partial t}, \tag{A5}$$

where α is a positive constant.

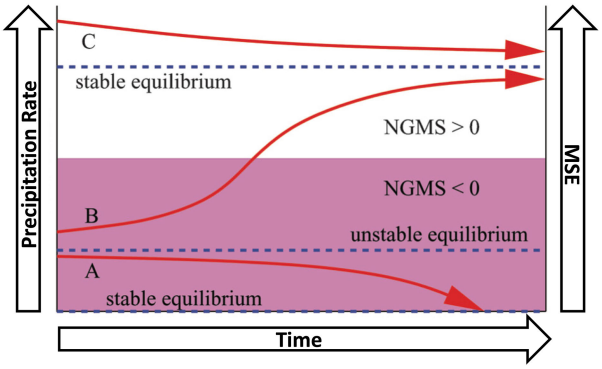

FIG. A1. Adapted from Raymond et al. (2009) Fig. 8. Assumes that normalized gross moist stability (NGMS) increases as precipitation rate increases, and that precipitation rate increases with increasing MSE. Curves A–C are examples of how the system may evolve in time.

To obtain an equation describing the temporal evolution of precipitation, both sides of Eq. (A2) are multiplied by Eq. (A3), giving

$$\Gamma \left\langle \frac{\partial \overline{q}}{\partial t} \right\rangle = \langle \overline{\mathbf{V}} \cdot \nabla \overline{h} \rangle + \left\langle \overline{\omega} \frac{\partial \overline{h}}{\partial p} \right\rangle + \Gamma E - \Gamma P. \tag{A6}$$

Next, Eq. (A4) is added to Eq. (A6), giving

$$(1 + \Gamma) \left\langle \frac{\partial \overline{q}}{\partial t} \right\rangle = (1 + \Gamma) E + H + \langle Q_r \rangle - \Gamma P. \tag{A7}$$

Finally, Eq. (A5) is substituted into Eq. (A7) to get

$$\left(\frac{1 + \Gamma}{\alpha} \right) \frac{\partial P}{\partial t} + \Gamma P = (1 + \Gamma) E + H + \langle Q_r \rangle. \tag{A8}$$

This is the full equation describing the temporal evolution of precipitation.

a. Equilibrium and perturbation precipitation equations

Define

$$P = P_{\text{eq}} + P_{\text{pert}}, \tag{A9}$$

where P_{eq} is the precipitation rate at an equilibrium state and P_{pert} is a precipitation perturbation from an equilibrium state. Similarly define

$$\Gamma = \Gamma_{\text{eq}} + \Gamma_{\text{pert}}, \tag{A10}$$

$$E = E_{\text{eq}} + E_{\text{pert}}, \tag{A11}$$

$$H = H_{\text{eq}} + H_{\text{pert}}, \tag{A12}$$

$$\langle Q_r \rangle = \langle Q_r \rangle_{\text{eq}} + \langle Q_r \rangle_{\text{pert}}. \tag{A13}$$

Findings of Inoue and Back (2017) showing both time-dependent and quasi-time-independent aspects of NGMS

provide some support for this separation. Using Eqs. (A9)–(A13) to expand Eq. (A8) gives

$$\left(\frac{1+\Gamma_{eq}+\Gamma_{pert}}{\alpha}\right)\frac{\partial(P_{eq}+P_{pert})}{\partial t}+(\Gamma_{eq}+\Gamma_{pert})(P_{eq}+P_{pert}) = (1+\Gamma_{eq}+\Gamma_{pert})(E_{eq}+E_{pert})H_{eq}+H_{pert} + \langle Q_r\rangle_{eq}+\langle Q_r\rangle_{pert}. \quad \text{(A14)}$$

Equation (A14) can now be separated into first-order (i.e., only X_{eq} terms and products of X_{eq} terms), second-order (i.e., only X_{pert} terms and products of X_{eq} and X_{pert} terms), and third-order (i.e., only products of X_{pert} and X_{pert} terms) equations, where the third-order equation will be dropped.

Recognizing that $\partial P_{eq}/\partial t = 0$, the first-order equation is given by

$$\Gamma_{eq}P_{eq} = (1+\Gamma_{eq})E_{eq}+H_{eq}+\langle Q_r\rangle_{eq}. \quad \text{(A15)}$$

Defining the diabatic source term D as

$$D = E + H + \langle Q_r\rangle. \quad \text{(A16)}$$

Equation (A15) can be rearranged to give

$$P_{eq} = E_{eq} + \frac{D_{eq}}{\Gamma_{eq}}, \quad \text{(A17)}$$

which describes precipitation at equilibrium. As noted by Raymond et al. (2009), net precipitation at equilibrium ($P_{eq} - E_{eq}$) is proportional to the diabatic forcing, and the smaller the NGMS, the larger the constant of proportionality, making understanding of NGMS a "prize worth pursuing."

The second-order equation is given by

$$\left(\frac{1+\Gamma_{eq}}{\alpha}\right)\frac{\partial P_{pert}}{\partial t}+\Gamma_{pert}P_{eq}+\Gamma_{eq}P_{pert} = (1+\Gamma_{eq})E_{pert}+E_{eq}\Gamma_{pert}+H_{pert}+\langle Q_r\rangle_{pert}. \quad \text{(A18)}$$

If it is *assumed* that feedbacks arising from perturbations in Γ, surface fluxes, and radiation can be neglected, such that

$$\Gamma_{pert} = E_{pert} = H_{pert} = \langle Q_r\rangle_{pert} = 0. \quad \text{(A19)}$$

Equation (A18) simplifies to

$$\frac{\partial P_{pert}}{\partial t} = -\frac{\alpha\Gamma_{eq}}{1+\Gamma_{eq}}P_{pert}, \quad \text{(A20)}$$

which describes the temporal evolution of precipitation perturbations away from an equilibrium state. Results from section 6 suggest that feedbacks arising from perturbations in Γ, surface fluxes, and radiation all play important roles in D–R cycles.

b. Stability of equilibrium states

Consider the following three scenarios, illustrated in Fig. A1, from Raymond et al. (2009):

1) If $\Gamma_{eq} > 0$, then Eq. (A20) shows that $\partial P_{pert}/\partial t$ will be of opposite sign of P_{pert}, indicating that both positive and negative precipitation perturbations will be returned back to their equilibrium values. This is a stable equilibrium associated with enhanced precipitation.
2) If $-1 < \Gamma_{eq} < 0$, then Eq. (A20) shows that $\partial P_{pert}/\partial t$ will have the same sign as P_{pert}, and both positive and negative precipitation perturbations will grow. This is an unstable equilibrium.
3) If $\Gamma_{eq} < -1$, then Eq. (A20) shows that $\partial P_{pert}/\partial t$ will be of opposite sign of P_{pert}, indicating that both positive and negative precipitation perturbations will be returned back to their equilibrium values. This is a stable equilibrium associated with suppressed precipitation.

APPENDIX B

Transition Time between D–R Cycles

Figure B1 shows the bin-mean number of days between D–R cycle transitions, where a subjectively chosen threshold of ($\langle B\rangle_{DIB} = -200$ J kg^{-1}) delineates shallow ($\langle B\rangle_{DIB} < -200$ J kg^{-1}) and deep ($\langle B\rangle_{DIB} > -200$ J kg^{-1}) convective D–R cycles. As might be expected, in general, the further conditions are from the threshold value, the longer the mean time until a transition occurs. For any fixed $\langle B\rangle_{DIB}$ value in the deep convective D–R cycle, higher precipitation rates are associated with shorter times until transition, suggesting that transitions are more likely to occur after widespread deep convective events than after periods of suppressed convection. In general, the shallow convective D–R cycle has shorter times until transition than the deep convective D–R cycle.

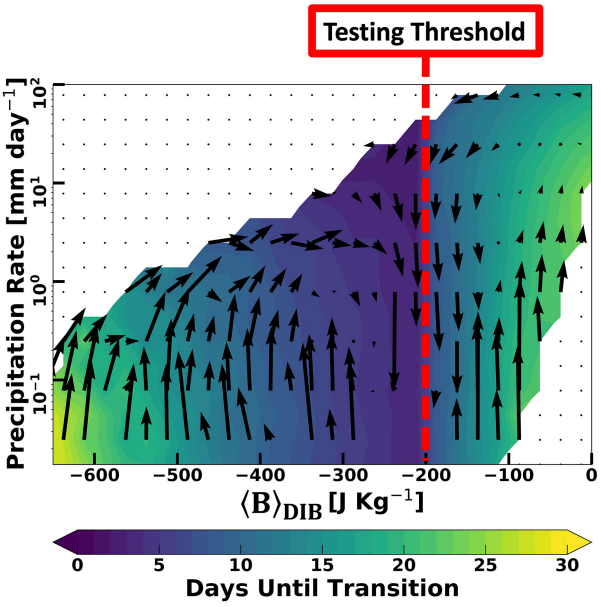

FIG. B1. As in Fig. 2b, except color shading shows the bin-mean number of days until a transition between the shallow and deep convective D–R cycles occurred. A subjectively chosen threshold of ($\langle B\rangle_{DIB} = -200$ J kg^{-1}) delineates shallow ($\langle B\rangle_{DIB} < -200$ J kg^{-1}) and deep ($\langle B\rangle_{DIB} > -200$ J kg^{-1}) convective D–R cycles.

APPENDIX C

Supplementary *CloudSat* Analysis

Analysis is as in section 4a, except showing the evolution of horizontal EO pixel composition instead of number of EOs (Fig. C1). Both analyses indicate a similar evolution of *CloudSat* cloud types during D–R cycles.

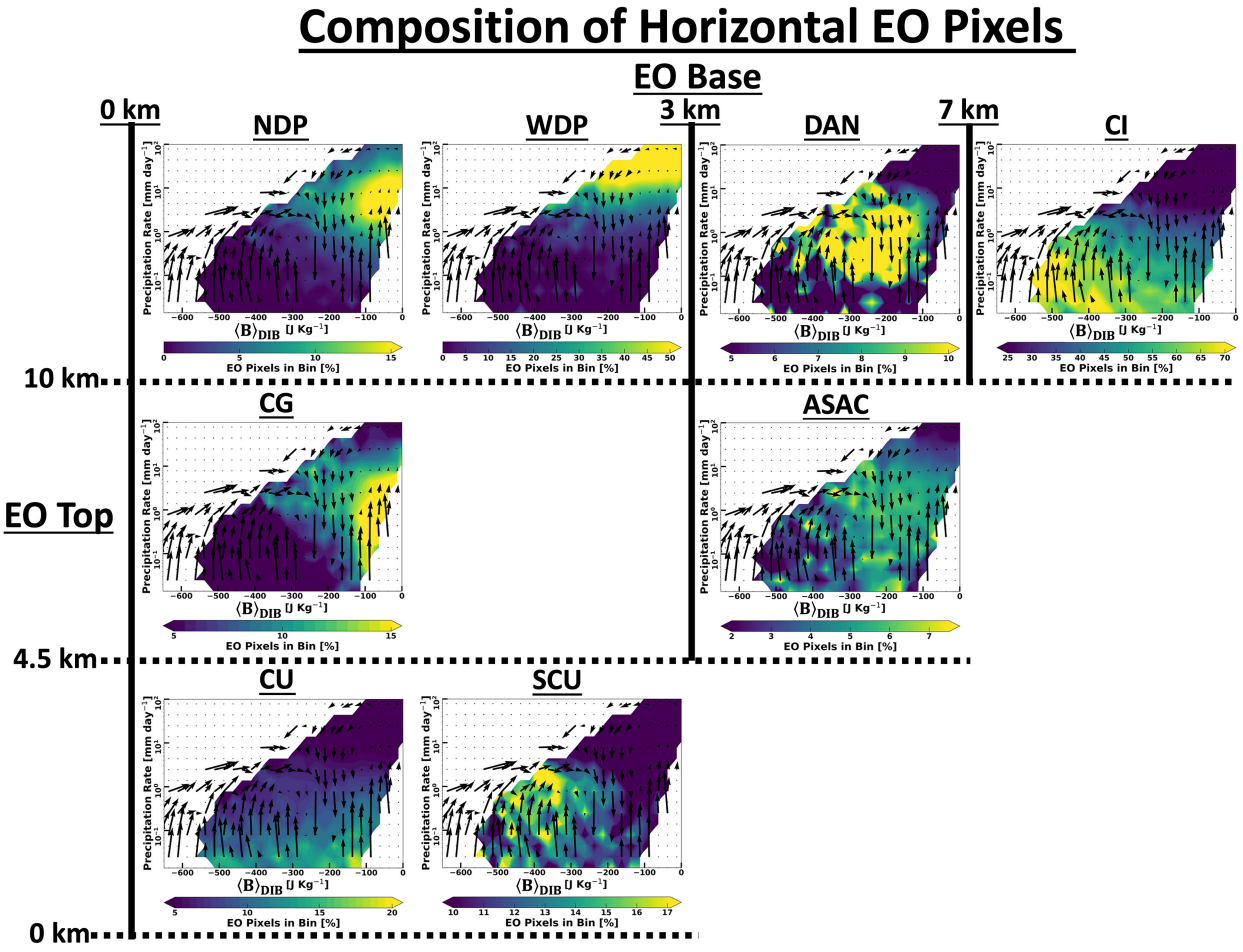

FIG. C1. As in Fig. 5, except color shading shows the fraction of horizontal EO pixels (BBWIDTHS variable) in each bin identified as shallow cumulus (CU), stratocumulus (SCU), cumulus congestus (CG), altostratus and altocumulus (ASAC), narrow deep precipitation (NDP), wide deep precipitation (WDP), detached anvil (DAN), and cirrus (CI) cloud types.

APPENDIX D

Examination of Bin-Mean $\langle B \rangle_{\text{NOMIX}}$ and $\langle B \rangle_{\text{MODENTRAIN}}$

Figure D1 shows that larger values of $\langle B \rangle_{\text{DIB}}$ (X axis) result from larger values of both $\langle B \rangle_{\text{NOMIX}}$ and $\langle B \rangle_{\text{MODENTRAIN}}$. The maximum in $\langle B \rangle_{\text{NOMIX}}$ occurs in the deep convective D–R cycle (D1), and is associated with enhanced cumulus (Fig. 5). The general increase in $\langle B \rangle_{\text{NOMIX}}$ with increasing $\langle B \rangle_{\text{DIB}}$ is the result of both increasing 1000 hPa moisture, and decreasing 800–600 hPa static stability. Increased 1000 hPa DSE contributes to the local maximum of $\langle B \rangle_{\text{NOMIX}}$ (D1).

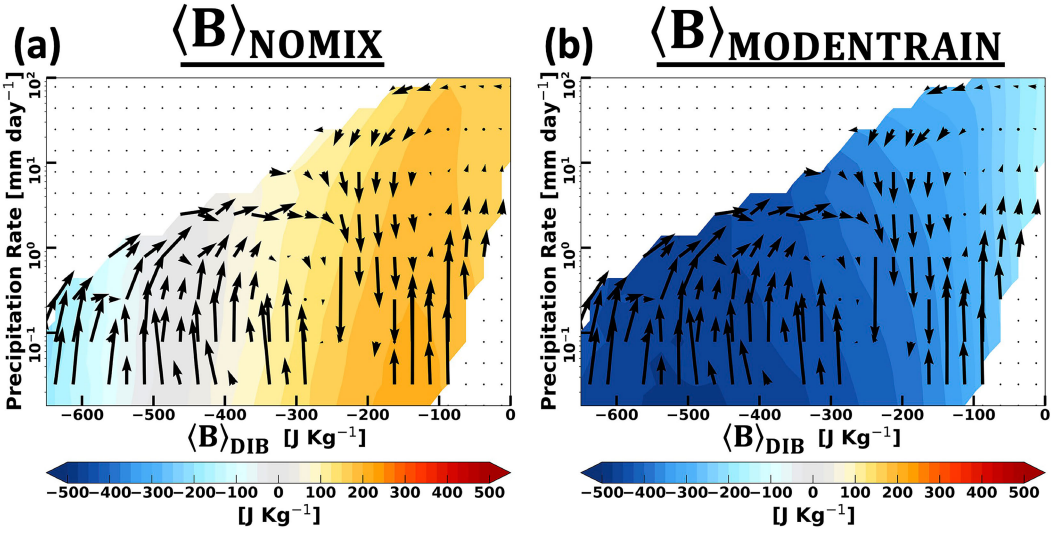

FIG. D1. As in Fig. 2b, except color shading shows bin-mean values of $\langle B \rangle_{\text{NOMIX}}$ and $\langle B \rangle_{\text{MODENTRAIN}}$.

REFERENCES

Adames, Á. F., and E. D. Maloney, 2021: Moisture mode theory's contribution to advances in our understanding of the Madden-Julian oscillation and other tropical disturbances. *Curr. Climate Change Rep.*, **7**, 72–85, https://doi.org/10.1007/s40641-021-00172-4.

——, S. W. Powell, F. Ahmed, V. C. Mayta, and J. D. Neelin, 2021: Tropical precipitation evolution in a buoyancy-budget framework. *J. Atmos. Sci.*, **78**, 509–528, https://doi.org/10.1175/JAS-D-20-0074.1.

Ahmed, F., and J. D. Neelin, 2018: Reverse engineering the tropical precipitation–buoyancy relationship. *J. Atmos. Sci.*, **75**, 1587–1608, https://doi.org/10.1175/JAS-D-17-0333.1.

——, and ——, 2021: Protected convection as a metric of dry air influence on precipitation. *J. Climate*, **34**, 3821–3838, https://doi.org/10.1175/JCLI-D-20-0384.1.

——, Á. F. Adames, and J. D. Neelin, 2020: Deep convective adjustment of temperature and moisture. *J. Atmos. Sci.*, **77**, 2163–2186, https://doi.org/10.1175/JAS-D-19-0227.1.

Angulo-Umana, P., and D. Kim, 2023: Mesoscale convective clustering enhances tropical precipitation. *Sci. Adv.*, **9**, eabo5317, https://doi.org/10.1126/sciadv.abo5317.

Arakawa, A., and W. H. Schubert, 1974: Interaction of a cumulus cloud ensemble with the large-scale environment, Part I. *J. Atmos. Sci.*, **31**, 674–701, https://doi.org/10.1175/1520-0469(1974)031<0674:IOACCE>2.0.CO;2.

Back, L. E., and C. S. Bretherton, 2006: Geographic variability in the export of moist static energy and vertical motion profiles in the tropical Pacific. *Geophys. Res. Lett.*, **33**, L17810, https://doi.org/10.1029/2006GL026672.

——, and ——, 2009: A simple model of climatological rainfall and vertical motion patterns over the tropical oceans. *J. Climate*, **22**, 6477–6497, https://doi.org/10.1175/2009JCLI2393.1.

Benedict, J. J., and D. A. Randall, 2007: Observed characteristics of the MJO relative to maximum rainfall. *J. Atmos. Sci.*, **64**, 2332–2354, https://doi.org/10.1175/JAS3968.1.

Bengtsson, L., J. Dias, S. Tulich, M. Gehne, and J.-W. Bao, 2021: A stochastic parameterization of organized tropical convection using cellular automata for global forecasts in NOAA's Unified Forecast System. *J. Adv. Model. Earth Syst.*, **13**, e2020MS002260, https://doi.org/10.1029/2020MS002260.

Bladé, I., and D. L. Hartmann, 1993: Tropical intraseasonal oscillations in a simple nonlinear model. *J. Atmos. Sci.*, **50**, 2922–2939, https://doi.org/10.1175/1520-0469(1993)050<2922:TIOIAS>2.0.CO;2.

Bony, S., H. Schulz, J. Vial, and B. Stevens, 2020a: Sugar, gravel, fish, and flowers: Dependence of mesoscale patterns of trade-wind clouds on environmental conditions. *Geophys. Res. Lett.*, **47**, e2019GL085988, https://doi.org/10.1029/2019GL085988.

——, A. Semie, R. J. Kramer, B. Soden, A. M. Tompkins, and K. A. Emanuel, 2020b: Observed modulation of the tropical radiation budget by deep convective organization and lower-tropospheric stability. *AGU Adv.*, **1**, e2019AV000155, https://doi.org/10.1029/2019AV000155.

Bretherton, C. S., and M. C. Wyant, 1997: Moisture transport, lower-tropospheric stability, and decoupling of cloud-topped boundary layers. *J. Atmos. Sci.*, **54**, 148–167, https://doi.org/10.1175/1520-0469(1997)054<0148:MTLTSA>2.0.CO;2.

Bryan, G. H., and J. M. Fritsch, 2004: A reevaluation of ice–liquid water potential temperature. *Mon. Wea. Rev.*, **132**, 2421–2431, https://doi.org/10.1175/1520-0493(2004)132<2421:AROIWP>2.0.CO;2.

Chen, S., and Coauthors, 2015: A study of CINDY/DYNAMO MJO suppressed phase. *J. Atmos. Sci.*, **72**, 3755–3779, https://doi.org/10.1175/JAS-D-13-0348.1.

Chen, S. S., and Coauthors, 2016: Aircraft observations of dry air, the ITCZ, convective cloud systems, and cold pools in MJO during DYNAMO. *Bull. Amer. Meteor. Soc.*, **97**, 405–423, https://doi.org/10.1175/BAMS-D-13-00196.1.

Chen, X., L. R. Leung, Z. Feng, and Q. Yang, 2022: Precipitation-moisture coupling over tropical oceans: Sequential roles of shallow, deep, and mesoscale convective systems. *Geophys. Res. Lett.*, **49**, e2022GL097836, https://doi.org/10.1029/2022GL097836.

Chikira, M., 2014: Eastward-propagating intraseasonal oscillation represented by Chikira–Sugiyama cumulus parameterization. Part II: Understanding moisture variation under weak temperature gradient balance. *J. Atmos. Sci.*, **71**, 615–639, https://doi.org/10.1175/JAS-D-13-038.1.

Chrisler, B., and J. P. Stachnik, 2021: The moist entropy budget of terminating Madden–Julian oscillation events. *J. Climate*, **34**, 4243–4260, https://doi.org/10.1175/JCLI-D-20-0064.1.

Ciesielski, P. E., R. H. Johnson, K. Yoneyama, and R. K. Taft, 2014a: Mitigation of Sri Lanka island effects in Colombo sounding data and its impact on DYNAMO analyses. *J. Meteor. Soc. Japan*, **92**, 385–405, https://doi.org/10.2151/jmsj.2014-407.

——, and Coauthors, 2014b: Quality-controlled upper-air sounding dataset for DYNAMO/CINDY/AMIE: Development and corrections. *J. Atmos. Oceanic Technol.*, **31**, 741–764, https://doi.org/10.1175/JTECH-D-13-00165.1.

de Szoeke, S. P., J. B. Edson, J. R. Marion, C. W. Fairall, and L. Bariteau, 2015: The MJO and air–sea interaction in TOGA COARE and DYNAMO. *J. Climate*, **28**, 597–622, https://doi.org/10.1175/JCLI-D-14-00477.1.

Donner, L. J., 1993: A cumulus parameterization including mass fluxes, vertical momentum dynamics, and mesoscale effects. *J. Atmos. Sci.*, **50**, 889–906, https://doi.org/10.1175/1520-0469(1993)050<0889:ACPIMF>2.0.CO;2.

Esbensen, S. K., and M. J. McPhaden, 1996: Enhancement of tropical ocean evaporation and sensible heat flux by atmospheric mesoscale systems. *J. Climate*, **9**, 2307–2325, https://doi.org/10.1175/1520-0442(1996)009<2307:EOTOEA>2.0.CO;2.

Feng, Z., and Coauthors, 2021: A global high-resolution mesoscale convective system database using satellite-derived cloud tops, surface precipitation, and tracking. *J. Geophys. Res. Atmos.*, **126**, e2020JD034202, https://doi.org/10.1029/2020JD034202.

Fuchs-Stone, Ž., D. J. Raymond, and S. Sentić, 2020: OTREC2019: Convection over the east Pacific and southwest Caribbean. *Geophys. Res. Lett.*, **47**, e2020GL087564, https://doi.org/10.1029/2020GL087564.

Hannah, W. M., B. E. Mapes, and G. S. Elsaesser, 2016: A Lagrangian view of moisture dynamics during DYNAMO. *J. Atmos. Sci.*, **73**, 1967–1985, https://doi.org/10.1175/JAS-D-15-0243.1.

Hartmann, D. L., L. A. Moy, and Q. Fu, 2001: Tropical convection and the energy balance at the top of the atmosphere. *J. Climate*, **14**, 4495–4511, https://doi.org/10.1175/1520-0442(2001)014<4495:TCATEB>2.0.CO;2.

Hersbach, H., and Coauthors, 2020: The ERA5 global reanalysis. *Quart. J. Roy. Meteor. Soc.*, **146**, 1999–2049, https://doi.org/10.1002/qj.3803.

Ho, S.-P., and Coauthors, 2020: The COSMIC/FORMOSAT-3 radio occultation mission after 12 years: Accomplishments, remaining challenges, and potential impacts of COSMIC-2. *Bull. Amer. Meteor. Soc.*, **101**, E1107–E1136, https://doi.org/10.1175/BAMS-D-18-0290.1.

Holloway, C. E., and J. D. Neelin, 2009: Moisture vertical structure, column water vapor, and tropical deep convection. *J. Atmos. Sci.*, **66**, 1665–1683, https://doi.org/10.1175/2008JAS2806.1.

Houze, R. A., Jr., 2004: Mesoscale convective systems. *Rev. Geophys.*, **42**, RG4003, https://doi.org/10.1029/2004RG000150.

——, 2018: 100 years of research on mesoscale convective systems. *A Century of Progress in Atmospheric and Related Sciences: Celebrating the American Meteorological Society Centennial*, *Meteor. Monogr.*, No. 59, Amer. Meteor. Soc., https://doi.org/10.1175/AMSMONOGRAPHS-D-18-0001.1.

Huffman, G. J., D. T. Bolvin, D. Braithwaite, K. Hsu, R. Joyce, P. Xie, and S.-H. Yoo, 2015: NASA Global Precipitation Measurement (GPM) Integrated Multi-satellitE Retrievals for GPM (IMERG). NASA Algorithm Theoretical Basis Doc., version 4, 26 pp.

Igel, M. R., 2017: The tropical precipitation pickup threshold and clouds in a radiative convective equilibrium model: 2. Two-layer moisture. *J. Geophys. Res. Atmos.*, **122**, 6469–6487, https://doi.org/10.1002/2016JD025908.

Inoue, K., and L. E. Back, 2017: Gross moist stability analysis: Assessment of satellite-based products in the GMS plane. *J. Atmos. Sci.*, **74**, 1819–1837, https://doi.org/10.1175/JAS-D-16-0218.1.

——, Á. F. Adames, and K. Yasunaga, 2020: Vertical velocity profiles in convectively coupled equatorial waves and MJO: New diagnoses of vertical velocity profiles in the wavenumber–frequency domain. *J. Atmos. Sci.*, **77**, 2139–2162, https://doi.org/10.1175/JAS-D-19-0209.1.

——, M. Biasutti, and A. M. Fridlind, 2021: Evidence that horizontal moisture advection regulates the ubiquitous amplification of rainfall variability over tropical oceans. *J. Atmos. Sci.*, **78**, 529–547, https://doi.org/10.1175/JAS-D-20-0201.1.

Jakob, C., M. S. Singh, and L. Jungandreas, 2019: Radiative convective equilibrium and organized convection: An observational perspective. *J. Geophys. Res. Atmos.*, **124**, 5418–5430, https://doi.org/10.1029/2018JD030092.

Janowiak, J., B. Joyce, and P. Xie, 2017: NCEP/CPC L3 half hourly 4km global (60S–60N) merged IR V1., version 1. GES DISC, accessed 27 February 2023, https://doi.org/10.5067/P4HZB9N27EKU.

Johnson, R., and P. Ciesielski, 2013: Evolution of MJO convection during DYNAMO deduced from the atmospheric sounding network. *EGU General Assembly 2013*, Vienna, Austria, Abstract 2115, https://meetingorganizer.copernicus.org/EGU2013/EGU2013-2115.pdf.

——, and ——, 2017: Multiscale variability of the atmospheric boundary layer during DYNAMO. *J. Atmos. Sci.*, **74**, 4003–4021, https://doi.org/10.1175/JAS-D-17-0182.1.

——, T. M. Rickenbach, S. A. Rutledge, P. E. Ciesielski, and W. H. Schubert, 1999: Trimodal characteristics of tropical convection. *J. Climate*, **12**, 2397–2418, https://doi.org/10.1175/1520-0442(1999)012<2397:TCOTC>2.0.CO;2.

——, P. E. Ciesielski, and J. A. Cotturone, 2001: Multiscale variability of the atmospheric mixed layer over the western

Pacific warm pool. *J. Atmos. Sci.*, **58**, 2729–2750, https://doi.org/10.1175/1520-0469(2001)058<2729:MVOTAM>2.0.CO;2.

——, ——, J. H. Ruppert Jr., and M. Katsumata, 2015: Sounding-based thermodynamic budgets for DYNAMO. *J. Atmos. Sci.*, **72**, 598–622, https://doi.org/10.1175/JAS-D-14-0202.1.

Khouider, B., and A. J. Majda, 2006: A simple multicloud parameterization for convectively coupled tropical waves. Part I: Linear analysis. *J. Atmos. Sci.*, **63**, 1308–1323, https://doi.org/10.1175/JAS3677.1.

Kiladis, G. N., M. C. Wheeler, P. T. Haertel, K. H. Straub, and P. E. Roundy, 2009: Convectively coupled equatorial waves. *Rev. Geophys.*, **47**, RG2003, https://doi.org/10.1029/2008RG000266.

Kingsmill, D. E., and R. A. Houze Jr., 1999: Thermodynamic characteristics of air flowing into and out of precipitating convection over the west Pacific warm pool. *Quart. J. Roy. Meteor. Soc.*, **125**, 1209–1229, https://doi.org/10.1002/qj.1999.49712555606.

Kuang, Z., 2008: A moisture-stratiform instability for convectively coupled waves. *J. Atmos. Sci.*, **65**, 834–854, https://doi.org/10.1175/2007JAS2444.1.

——, 2010: Linear response functions of a cumulus ensemble to temperature and moisture perturbations and implications for the dynamics of convectively coupled waves. *J. Atmos. Sci.*, **67**, 941–962, https://doi.org/10.1175/2009JAS3260.1.

Kumar, V. V., C. Jakob, A. Protat, C. R. Williams, and P. T. May, 2015: Mass-flux characteristics of tropical cumulus clouds from wind profiler observations at Darwin, Australia. *J. Atmos. Sci.*, **72**, 1837–1855, https://doi.org/10.1175/JAS-D-14-0259.1.

Kuo, Y.-H., and J. D. Neelin, 2022: Conditions for convective deep inflow. *Geophys. Res. Lett.*, **49**, e2022GL100552, https://doi.org/10.1029/2022GL100552.

Maithel, V., and L. Back, 2022: Moisture recharge–discharge cycles: A gross moist stability–based phase angle perspective. *J. Atmos. Sci.*, **79**, 2401–2417, https://doi.org/10.1175/JAS-D-21-0297.1.

Maloney, E. D., 2009: The moist static energy budget of a composite tropical intraseasonal oscillation in a climate model. *J. Climate*, **22**, 711–729, https://doi.org/10.1175/2008JCLI2542.1.

——, and B. O. Wolding, 2015: Initiation of an intraseasonal oscillation in an aquaplanet general circulation model. *J. Adv. Model. Earth Syst.*, **7**, 1956–1976, https://doi.org/10.1002/2015MS000495.

Mapes, B. E., 1993: Gregarious tropical convection. *J. Atmos. Sci.*, **50**, 2026–2037, https://doi.org/10.1175/1520-0469(1993)050<2026:GTC>2.0.CO;2.

——, 2000: Convective inhibition, subgrid-scale triggering energy, and stratiform instability in a toy tropical wave model. *J. Atmos. Sci.*, **57**, 1515–1535, https://doi.org/10.1175/1520-0469(2000)057<1515:CISSTE>2.0.CO;2.

——, and R. Neale, 2011: Parameterizing convective organization to escape the entrainment dilemma. *J. Adv. Model. Earth Syst.*, **3**, M06004, https://doi.org/10.1029/2011MS000042.

——, S. Tulich, J. Lin, and P. Zuidema, 2006: The mesoscale convection life cycle: Building block or prototype for large-scale tropical waves? *Dyn. Atmos. Oceans*, **42**, 3–29, https://doi.org/10.1016/j.dynatmoce.2006.03.003.

Masunaga, H., and T. S. L'Ecuyer, 2014: A mechanism of tropical convection inferred from observed variability in the moist static energy budget. *J. Atmos. Sci.*, **71**, 3747–3766, https://doi.org/10.1175/JAS-D-14-0015.1.

Matthews, A. J., 2008: Primary and successive events in the Madden–Julian oscillation. *Quart. J. Roy. Meteor. Soc.*, **134**, 439–453, https://doi.org/10.1002/qj.224.

McCoy, I. L., D. T. McCoy, R. Wood, P. Zuidema, and F. A.-M. Bender, 2023: The role of mesoscale cloud morphology in the shortwave cloud feedback. *Geophys. Res. Lett.*, **50**, e2022GL101042, https://doi.org/10.1029/2022GL101042.

McGee, C. J., and S. C. van den Heever, 2014: Latent heating and mixing due to entrainment in tropical deep convection. *J. Atmos. Sci.*, **71**, 816–832, https://doi.org/10.1175/JAS-D-13-0140.1.

Mechem, D. B., R. A. Houze Jr., and S. S. Chen, 2002: Layer inflow into precipitating convection over the western tropical Pacific. *Quart. J. Roy. Meteor. Soc.*, **128**, 1997–2030, https://doi.org/10.1256/003590002320603502.

Moncrieff, M. W., 2004: Analytic representation of the large-scale organization of tropical convection. *J. Atmos. Sci.*, **61**, 1521–1538, https://doi.org/10.1175/1520-0469(2004)061<1521:AROTLO>2.0.CO;2.

——, C. Liu, and P. Bogenschutz, 2017: Simulation, modeling, and dynamically based parameterization of organized tropical convection for global climate models. *J. Atmos. Sci.*, **74**, 1363–1380, https://doi.org/10.1175/JAS-D-16-0166.1.

Neelin, J. D., O. Peters, J. W.-B. Lin, K. Hales, and C. E. Holloway, 2008: Rethinking convective quasi-equilibrium: Observational constraints for stochastic convective schemes in climate models. *Philos. Trans. Roy. Soc.*, **A366**, 2579–2602, https://doi.org/10.1098/rsta.2008.0056.

——, ——, and K. Hales, 2009: The transition to strong convection. *J. Atmos. Sci.*, **66**, 2367–2384, https://doi.org/10.1175/2009JAS2962.1.

Park, S., 2014: A unified convection scheme (UNICON). Part I: Formulation. *J. Atmos. Sci.*, **71**, 3902–3930, https://doi.org/10.1175/JAS-D-13-0233.1.

Peters, J. M., H. Morrison, A. C. Varble, W. M. Hannah, and S. E. Giangrande, 2020: Thermal chains and entrainment in cumulus updrafts. Part II: Analysis of idealized simulations. *J. Atmos. Sci.*, **77**, 3661–3681, https://doi.org/10.1175/JAS-D-19-0244.1.

——, ——, G. J. Zhang, and S. Powell, 2021: Improving the physical basis for updraft dynamics in deep convection parameterizations. *J. Adv. Model. Earth Syst.*, **13**, e2020MS002282, https://doi.org/10.1029/2020MS002282.

Peters, O., and J. D. Neelin, 2006: Critical phenomena in atmospheric precipitation. *Nat. Phys.*, **2**, 393–396, https://doi.org/10.1038/nphys314.

Pincus, R., A. Beljaars, S. A. Buehler, G. Kirchengast, F. Ladstaedter, and J. S. Whitaker, 2017: The representation of tropospheric water vapor over low-latitude oceans in (re-)analysis: Errors, impacts, and the ability to exploit current and prospective observations. *Surv. Geophys.*, **38**, 1399–1423, https://doi.org/10.1007/s10712-017-9437-z.

Poli, P., S. B. Healy, and D. P. Dee, 2010: Assimilation of global positioning system radio occultation data in the ECMWF ERA-Interim reanalysis. *Quart. J. Roy. Meteor. Soc.*, **136**, 1972–1990, https://doi.org/10.1002/qj.722.

Powell, S. W., 2019: Observing possible thermodynamic controls on tropical marine rainfall in moist environments. *J. Atmos. Sci.*, **76**, 3737–3751, https://doi.org/10.1175/JAS-D-19-0144.1.

Randall, D., 2015: *An Introduction to the Global Circulation of the Atmosphere*. Princeton University Press, 454 pp.

Raymond, D. J., 1997: Boundary layer quasi-equilibrium (BLQ). *The Physics and Parameterization of Moist Atmospheric Convection*, Springer, 387–397.

——, 2000: Thermodynamic control of tropical rainfall. *Quart. J. Roy. Meteor. Soc.*, **126**, 889–898, https://doi.org/10.1002/qj.49712656406.

——, 2001: A new model of the Madden–Julian oscillation. *J. Atmos. Sci.*, **58**, 2807–2819, https://doi.org/10.1175/1520-0469(2001)058<2807:ANMOTM>2.0.CO;2.

——, and Ž. Fuchs-Stone, 2021: Emergent properties of convection in OTREC and PREDICT. *J. Geophys. Res. Atmos.*, **126**, e2020JD033585, https://doi.org/10.1029/2020JD033585.

——, G. B. Raga, C. S. Bretherton, J. Molinari, C. López-Carrillo, and Ž. Fuchs, 2003: Convective forcing in the intertropical convergence zone of the eastern Pacific. *J. Atmos. Sci.*, **60**, 2064–2082, https://doi.org/10.1175/1520-0469(2003)060<2064:CFITIC>2.0.CO;2.

——, S. L. Sessions, A. H. Sobel, and Ž. Fuchs, 2009: The mechanics of gross moist stability. *J. Adv. Model. Earth Syst.*, **1** (3), https://doi.org/10.3894/JAMES.2009.1.9.

——, ——, and C. López Carrillo, 2011: Thermodynamics of tropical cyclogenesis in the northwest Pacific. *J. Geophys. Res.*, **116**, D18101, https://doi.org/10.1029/2011JD015624.

Ren, P., D. Kim, M.-S. Ahn, D. Kang, and H.-L. Ren, 2021: Intercomparison of MJO column moist static energy and water vapor budget among six modern reanalysis products. *J. Climate*, **34**, 2977–3001, https://doi.org/10.1175/JCLI-D-20-0653.1.

Riley, E. M., and B. E. Mapes, 2009: Unexpected peak near −15°C in CloudSat echo top climatology. *Geophys. Res. Lett.*, **36**, L09819, https://doi.org/10.1029/2009GL037558.

——, and ——, 2023: Data for: Attributes of CloudSat identified echo objects. Dryad, accessed 27 February 2023, https://doi.org/10.5061/dryad.jdfn2z3fm.

——, ——, and S. N. Tulich, 2011: Clouds associated with the Madden–Julian oscillation: A new perspective from *CloudSat*. *J. Atmos. Sci.*, **68**, 3032–3051, https://doi.org/10.1175/JAS-D-11-030.1.

Ruppert, J. H., Jr., and R. H. Johnson, 2015: Diurnally modulated cumulus moistening in the preonset stage of the Madden–Julian oscillation during DYNAMO. *J. Atmos. Sci.*, **72**, 1622–1647, https://doi.org/10.1175/JAS-D-14-0218.1.

Rydbeck, A. V., and Coauthors, 2023: Anchoring intraseasonal air–sea interactions: The moored moist static energy budget in the Indian Ocean from reanalysis. *J. Climate*, **36**, 959–981, https://doi.org/10.1175/JCLI-D-22-0182.1.

Sahany, S., J. D. Neelin, K. Hales, and R. B. Neale, 2012: Temperature–moisture dependence of the deep convective transition as a constraint on entrainment in climate models. *J. Atmos. Sci.*, **69**, 1340–1358, https://doi.org/10.1175/JAS-D-11-0164.1.

Schiro, K. A., F. Ahmed, S. E. Giangrande, and J. D. Neelin, 2018: GoAmazon2014/5 campaign points to deep-inflow approach to deep convection across scales. *Proc. Natl. Acad. Sci. USA*, **115**, 4577–4582, https://doi.org/10.1073/pnas.1719842115.

——, S. C. Sullivan, Y.-H. Kuo, H. Su, P. Gentine, G. S. Elsaesser, J. H. Jiang, and J. D. Neelin, 2020: Environmental controls on tropical mesoscale convective system precipitation intensity. *J. Atmos. Sci.*, **77**, 4233–4249, https://doi.org/10.1175/JAS-D-20-0111.1.

Schulz, H., R. Eastman, and B. Stevens, 2021: Characterization and evolution of organized shallow convection in the downstream North Atlantic trades. *J. Geophys. Res. Atmos.*, **126**, e2021JD034575, https://doi.org/10.1029/2021JD034575.

Schumacher, C., R. A. Houze Jr., and I. Kraucunas, 2004: The tropical dynamical response to latent heating estimates derived from the TRMM Precipitation Radar. *J. Atmos. Sci.*, **61**, 1341–1358, https://doi.org/10.1175/1520-0469(2004)061<1341:TTDRTL>2.0.CO;2.

Sentić, S., P. Bechtold, Ž. Fuchs-Stone, M. Rodwell, and D. J. Raymond, 2022: On the impact of dropsondes on the ECMWF Integrated Forecasting System model (CY47R1) analysis of convection during the OTREC (Organization of Tropical East Pacific Convection) field campaign. *Geosci. Model Dev.*, **15**, 3371–3385, https://doi.org/10.5194/gmd-15-3371-2022.

Serra, Y. L., S. A. Rutledge, K. Chudler, and C. Zhang, 2023: Rainfall and convection in ERA5 and MERRA-2 over the northern equatorial western Pacific during PISTON. *J. Climate*, **36**, 845–863, https://doi.org/10.1175/JCLI-D-22-0203.1.

Sessions, S. L., S. Sugaya, D. J. Raymond, and A. H. Sobel, 2010: Multiple equilibria in a cloud-resolving model using the weak temperature gradient approximation. *J. Geophys. Res.*, **115**, D12110, https://doi.org/10.1029/2009JD013376.

Shamekh, S., K. D. Lamb, Y. Huang, and P. Gentine, 2023: Implicit learning of convective organization explains precipitation stochasticity. *Proc. Natl. Acad. Sci. USA*, **120**, e2216158120, https://doi.org/10.1073/pnas.2216158120.

Sobel, A. H., and C. S. Bretherton, 2000: Modeling tropical precipitation in a single column. *J. Climate*, **13**, 4378–4392, https://doi.org/10.1175/1520-0442(2000)013<4378:MTPIAS>2.0.CO;2.

——, J. Nilsson, and L. M. Polvani, 2001: The weak temperature gradient approximation and balanced tropical moisture waves. *J. Atmos. Sci.*, **58**, 3650–3665, https://doi.org/10.1175/1520-0469(2001)058<3650:TWTGAA>2.0.CO;2.

——, G. Bellon, and J. Bacmeister, 2007: Multiple equilibria in a single-column model of the tropical atmosphere. *Geophys. Res. Lett.*, **34**, L22804, https://doi.org/10.1029/2007GL031320.

——, S. Wang, and D. Kim, 2014: Moist static energy budget of the MJO during DYNAMO. *J. Atmos. Sci.*, **71**, 4276–4291, https://doi.org/10.1175/JAS-D-14-0052.1.

Stachnik, J. P., D. E. Waliser, and A. J. Majda, 2015: Precursor environmental conditions associated with the termination of Madden–Julian oscillation events. *J. Atmos. Sci.*, **72**, 1908–1931, https://doi.org/10.1175/JAS-D-14-0254.1.

Stephens, G. L., and Coauthors, 2010: Dreary state of precipitation in global models. *J. Geophys. Res.*, **115**, D24211, https://doi.org/10.1029/2010JD014532.

Straub, K. H., 2013: MJO initiation in the real-time multivariate MJO index. *J. Climate*, **26**, 1130–1151, https://doi.org/10.1175/JCLI-D-12-00074.1.

Tan, J., G. J. Huffman, D. T. Bolvin, and E. J. Nelkin, 2019: IMERG V06: Changes to the morphing algorithm. *J. Atmos. Oceanic Technol.*, **36**, 2471–2482, https://doi.org/10.1175/JTECH-D-19-0114.1.

Tobin, I., S. Bony, and R. Roca, 2012: Observational evidence for relationships between the degree of aggregation of deep convection, water vapor, surface fluxes, and radiation. *J. Climate*, **25**, 6885–6904, https://doi.org/10.1175/JCLI-D-11-00258.1.

Tompkins, A. M., and A. G. Semie, 2017: Organization of tropical convection in low vertical wind shears: Role of updraft entrainment. *J. Adv. Model. Earth Syst.*, **9**, 1046–1068, https://doi.org/10.1002/2016MS000802.

Tulich, S. N., and B. E. Mapes, 2010: Transient environmental sensitivities of explicitly simulated tropical convection. *J. Atmos. Sci.*, **67**, 923–940, https://doi.org/10.1175/2009JAS3277.1.

Wang, S., A. H. Sobel, and J. Nie, 2016: Modeling the MJO in a cloud-resolving model with parameterized large-scale dynamics: Vertical structure, radiation, and horizontal advection of dry air. *J. Adv. Model. Earth Syst.*, **8**, 121–139, https://doi.org/10.1002/2015MS000529.

Wolding, B. O., and E. D. Maloney, 2015: Objective diagnostics and the Madden–Julian oscillation. Part II: Application to moist static energy and moisture budgets. *J. Climate*, **28**, 7786–7808, https://doi.org/10.1175/JCLI-D-14-00689.1.

——, J. Dias, G. Kiladis, F. Ahmed, S. W. Powell, E. Maloney, and M. Branson, 2020a: Interactions between moisture and tropical convection. Part I: The coevolution of moisture and convection. *J. Atmos. Sci.*, **77**, 1783–1799, https://doi.org/10.1175/JAS-D-19-0225.1.

——, ——, ——, E. Maloney, and M. Branson, 2020b: Interactions between moisture and tropical convection. Part II: The convective coupling of equatorial waves. *J. Atmos. Sci.*, **77**, 1801–1819, https://doi.org/10.1175/JAS-D-19-0226.1.

——, S. W. Powell, F. Ahmed, J. Dias, M. Gehne, G. Kiladis, and J. D. Neelin, 2022: Tropical thermodynamic–convection coupling in observations and reanalyses. *J. Atmos. Sci.*, **79**, 1781–1803, https://doi.org/10.1175/JAS-D-21-0256.1.

Wood, R., 2012: Stratocumulus clouds. *Mon. Wea. Rev.*, **140**, 2373–2423, https://doi.org/10.1175/MWR-D-11-00121.1.

——, and C. S. Bretherton, 2004: Boundary layer depth, entrainment, and decoupling in the cloud-capped subtropical and tropical marine boundary layer. *J. Climate*, **17**, 3576–3588, https://doi.org/10.1175/1520-0442(2004)017<3576:BLDEAD>2.0.CO;2.

Xie, F., D. L. Wu, C. O. Ao, A. J. Mannucci, and E. R. Kursinski, 2012: Advances and limitations of atmospheric boundary layer observations with GPS occultation over southeast Pacific Ocean. *Atmos. Chem. Phys.*, **12**, 903–918, https://doi.org/10.5194/acp-12-903-2012.

Yano, J.-I., and R. Plant, 2012a: Finite departure from convective quasi-equilibrium: Periodic cycle and discharge–recharge mechanism. *Quart. J. Roy. Meteor. Soc.*, **138**, 626–637, https://doi.org/10.1002/qj.957.

——, and ——, 2012b: Interactions between shallow and deep convection under a finite departure from convective quasi equilibrium. *J. Atmos. Sci.*, **69**, 3463–3470, https://doi.org/10.1175/JAS-D-12-0108.1.

——, M. H. Ambaum, H. F. Dacre, and A. Manzato, 2020: A dynamical–system description of precipitation over the tropics and the midlatitudes. *Tellus*, **72A**, 1847939, https://doi.org/10.1080/16000870.2020.1847939.

Yoneyama, K., C. Zhang, and C. N. Long, 2013: Tracking pulses of the Madden–Julian oscillation. *Bull. Amer. Meteor. Soc.*, **94**, 1871–1891, https://doi.org/10.1175/BAMS-D-12-00157.1.

Zhang, C., 2013: Madden–Julian oscillation: Bridging weather and climate. *Bull. Amer. Meteor. Soc.*, **94**, 1849–1870, https://doi.org/10.1175/BAMS-D-12-00026.1.

——, and K. Yoneyama, 2017: CINDY/DYNAMO field campaign: Advancing our understanding of MJO initiation. *The Global Monsoon System: Research and Forecast*, World Scientific, 339–348.

Zhang, G. J., 2009: Effects of entrainment on convective available potential energy and closure assumptions in convection parameterization. *J. Geophys. Res.*, **114**, D07109, https://doi.org/10.1029/2008JD010976.

Zipser, E. J., 1977: Mesoscale and convective-scale downdrafts as distinct components of squall-line structure. *Mon. Wea. Rev.*, **105**, 1568–1589, https://doi.org/10.1175/1520-0493(1977)105<1568:MACDAD>2.0.CO;2.